DETERMINATION OF THE AIR AND CROP FLOW BEHAVIOUR IN THE BLOWING UNIT AND SPOUT OF A PULL-TYPE FORAGE HARVESTER

A Thesis Submitted to the
College of Graduate Studies and Research
in Partial Fulfilment of the Requirements
for the Degree of Master of Science in the
Department of Agricultural and Bioresource Engineering

University of Saskatchewan
Saskatoon
Saskatchewan

By
Dennis Lammers

PERMISSION TO USE

In presenting this thesis in partial fulfillment of the requirements for a degree of Master of Science from the University of Saskatchewan, I agree that the libraries of this University may make it freely available for inspection. I further agree that permission for copying this thesis in any manner, in whole or in part for scholarly purposes may be granted by the professor who supervised my thesis work or, in his absence, by the Head of the Department or the Dean of the College in which my thesis work was done. Copying or publication or use of this thesis or parts thereof for financial gain without the author's written permission is prohibited. It is understood that due recognition shall be given to the author and to the University of Saskatchewan for any scholarly use of material contained in this thesis.

Requests for permission to copy or to make other use of material in this thesis in whole or in part should be addressed to:

Head of the Department of Agricultural and Bioresource Engineering

University of Saskatchewan
57 Campus Drive
Saskatoon, SK. Canada
S7N 5A9

ABSTRACT

The energy requirements of forage harvesters can be quite high and can sometimes determine the size of tractor needed on a farm. Therefore, improving the energy efficiency of the forage harvester could allow a farm to reduce costs by using a smaller tractor that is less expensive and more efficient. The objective of this research was to increase the throwing distance of a forage harvester by modeling the flow of forage in the spout and the air flow in the blower and spout. These models can then be used to compare the efficiencies of prototype designs.

The air flow in the blower and spout was modeled using the commercial computational fluid dynamics software FLUENT. The simulation results of air velocities and flow patterns were compared to experimental values and it was found that both were of the same order of magnitude with the model predicting slightly higher air velocities than those measured.

The flow of forage in the spout was modeled analytically by taking into account the friction between the forage and the spout surface and the aerodynamic resistance after the forage leaves the spout. From this model, two improved prototype spouts that should theoretically result in longer throwing distances were designed. However, field testing of the two prototypes did not reveal any significant improvements over the current design. It was also found that the model under-predicted the throwing distance of one prototype by 2 % and over estimated the other by 12 %.

ACKNOWLEDGEMENTS

I would like to acknowledge the guidance I have received from my supervisor Dr. Martin Roberge which has been instrumental in the completion of this project. I would also like to thank the members of my committee, Dr. Charles Maule, Dr. Claude Laguë and Dr. Trever Crowe.

This project was made possible by the support of Dion Machineries Inc. through funding and equipment. Finally I would like to thank the organizations that provided financial support to me through the course of my graduate studies.

DEDICATION

I would like to dedicate this work to my parents who didn't get the opportunity to see the completion of, but had an immeasurable role in making me who I am today which allowed me to complete this accomplishment.

TABLE OF CONTENTS

LIST OF FIGURES

LIST OF TABLES

LIST OF ABBREVIATIONS

$\vec{A}$:	surface area vector
$\vec{A}_f$:	area of face f
A_p:	cross sectional area of the body normal to the flow
BC:	boundary condition
CFD	computational fluid dynamics
c_w:	drag coefficient
d_A:	mean equivalent diameter of particle
$\vec{F}$:	external body forces
f:	coefficient of friction
fps	frames per second
g:	acceleration of gravity
I:	unit tensor
K:	aerodynamic coefficient
K_1:	aerodynamic coefficient
KE_L:	kinetic energy lost
k:	turbulence kinetic energy per unit mass
m:	mass of the particle
Nfaces:	number of faces enclosing control volume
p:	static pressure
r:	radius of curvature
S_ϕ:	source of ϕ per unit volume
S_m:	mass added to the continuous phase
s:	tangential position of particle in spout measured from the horizontal
s_o:	initial tangential position of particle in spout measured from the horizontal
t:	time
V:	volume of control volume
$\vec{v}$:	velocity vector

v_{dens}:	density of particles
v_m:	mean velocity during impact
v_{o1}:	initial velocity of the particle
v_{o2}:	initial tangential velocity of the particle
v_{o3}:	initial velocity of the particle
W_{df}:	drag force
W_x:	horizontal component of drag force
W_y:	vertical component of drag force
X	X coordinate direction
x:	horizontal position
Y	Y coordinate direction
y:	vertical position
Z	Z coordinate direction
α_{throw}:	angle particles leave the spout
Γ_ϕ:	diffusion coefficient for ϕ
ε:	turbulence dissipation rate per unit mass
θ:	angle of the inclined plane
μ:	molecular viscosity
ρ:	density
ρ_A:	air density
$\rho\vec{g}$:	gravitational body force
$\rho_f \vec{v}_f \cdot \vec{A}_f$:	mass flux through the face
$\overline{\overline{\tau}}$:	stress tensor
ϕ:	scalar quantity
ϕ_f:	value of ϕ convected through face f
∇:	gradient
$(\nabla\phi)_n$:	magnitude of $\nabla\phi$ normal to face f

1 INTRODUCTION

Forage harvesters are used on farms to harvest crops to be used as animal feed. The crops are harvested when they are green, producing a high-quality animal feed known as green feed or silage. Many different crops are harvested this way including corn, timothy grass, alfalfa and various cereal crops. The basic operation of a forage harvester consists of the following functions (Kepner et al., 1978):

1. a gathering unit to cut standing plants or to pick up windrowed material,
2. a conveying and feed mechanism with spring-loaded rolls or aprons to compress and hold the material for chopping,
3. a cutterhead or chopping unit and
4. a conveying or impelling arrangement to deposit the chopped material in the transport vehicle.

The conveying arrangement uses either the kinetic energy produced by the cutterhead (cut-and-throw) or by an auxiliary blower (cut-and-blow) to accelerate the forage. Figure 1.1 shows an example of a pull-type cut-and-blow forage harvester with the major components labeled.

There were approximately 475 pull-type and self-propelled forage harvesters sold in Canada annually from 1991 to 2001 (Nieuwenhof, 2003). The energy requirements of pull-type forage harvesters can be quite high, with specific energies as high as 3.5 kWh/t, which can sometimes determine the size of tractor needed on a farm (Shinners et al.,

1994). Therefore, reducing the energy consumption of the forage harvester is of great interest.

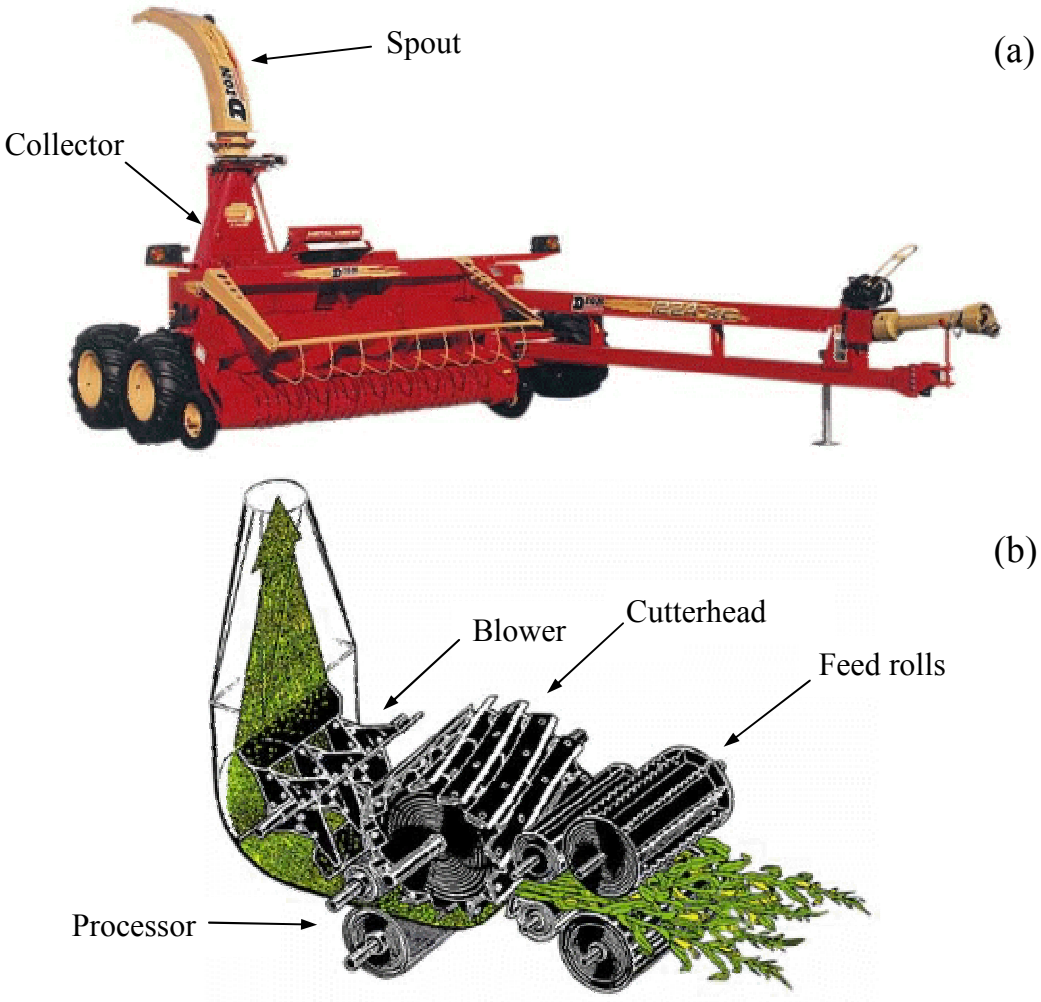

Figure 1.1 Example of pull-type forage harvester, a, with identification of major components, b.

Note. From Development Forage Equipment Inc.. Available from D.F.E. Inc. website, http://www.dionmachineries.com/f41a.htm. Reprinted with permission.

This research will involve both the flow of forage in the spout and the air flow in the blower and spout. Two models were developed in the course of this project to describe

the air and forage flow: a numerical model of the air flow using computational fluid dynamics (CFD) software, and an analytical model to predict the distance forage is thrown from the spout. The analytical model can be used to compare different spout designs and the numerical model can be used to predict air flow patterns and velocities of different fan and housing designs.

The body of this thesis consists of seven chapters including this introduction. Chapter 2 is a literature review of relevant research and Chapter 3 outlines the objectives of this research. Chapters 4 and 5 outline the air flow and forage flow models respectively. Chapter 6 provides the conclusions derived from this research, and Chapter 7 lists the references cited.

2 LITERATURE REVIEW

A review of the literature pertaining to forage harvesters has shown much research on improving their efficiency. A major improvement was made by Shinners et al. (1991a) by inverting the cutterhead of a cut-and-throw forage harvester from its normal position (downward cutting) so the knives enter the uncut forage from underneath (upward cutting). This configuration reduced the specific energy requirements by 30% and 34% compared to conventional cut-and-throw and cut-and-blow configurations, respectively.

Shinners et al. (1994) attempted to improve the throwing distance of the upward cutting forage harvester that was 27% shorter than a conventional cut-and-blow forage harvester. The air flow to the cutterhead was increased by increasing the open area in the sides of the cutterhead housing. This increased the air velocity and improved the throwing distance. Throwing counter surfaces were also mounted perpendicular and inboard to the knife (Figure 2.1) that also helped to improve the throwing effectiveness.

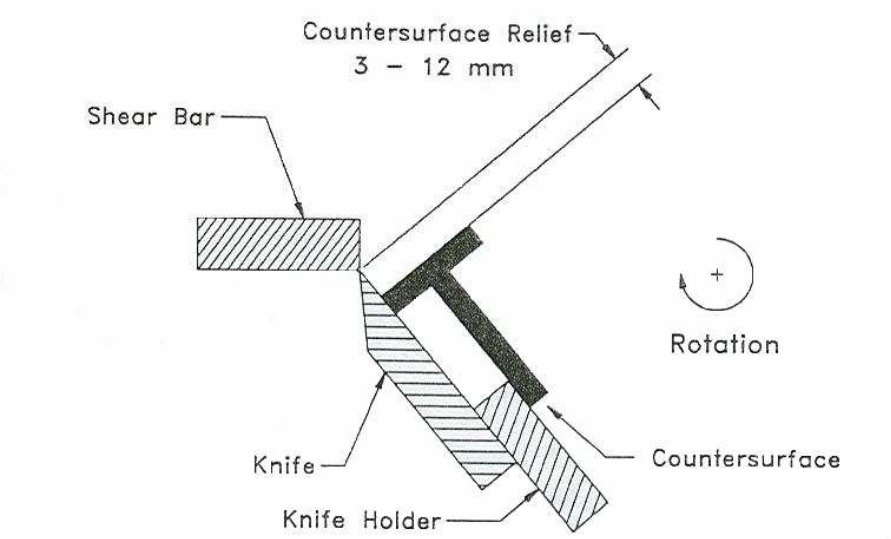

Figure 2.1 Throwing counter surface design used by Shinners et al. (1994) to improve throwing effectiveness.

Research was also conducted by Shinners et al. (1991b) into reducing the friction in forage blowers through band lubrication. It was found that the specific energy requirement of the blower was reduced by 26% with the spray application of water.

The reduction of peak power of a forage harvester through the use of a flywheel was examined by Tremblay et al. (1991). It was found that the flywheel reduced the instantaneous peak power by 6% in irregular windrows and 20% in regular windrows. It was also predicted that these reductions should increase harvest capacity by 3% to 4%.

Past research summarized by Shinners et al. (1991) separated the energy requirements within a forage harvester as approximately: 40% for pneumatic conveying, 40% for the cutterhead and 20% for material pick-up and drive train losses. The blower which provides the energy for pneumatic conveying is a large percentage of the machine's

energy requirements and therefore would be a good area to improve the efficiency of the harvester.

Pneumatic conveying was described by Stoess (1983) as the art of transporting bulk materials through a pipeline by either a negative or a positive pressure air-stream. Transporting bulk materials by pneumatic conveying has been used by many industries including the cement, baking, plastics, powder and feed industries to list a few (Stoess, 1983). A sample of some of the research on pneumatic conveying systems found is given here.

Research into the effect of bends on the flow of granular materials in a pneumatic conveying system was conducted by Lee et al. (2004). Solid concentrations and velocity distributions were measured and numerical simulation was used to model fluid and particle flow characteristics. Levy and Mason (1998) also examined particle flow in a bend using a numerical model to determine particle concentrations and segregation. The effect of bend radius and air velocity on damage to feed pellets was investigated by Aarseth (2004).

Optimization of pneumatic a conveying system to increase efficiency was studied by Baker and Klinzing (1999). The two methods used for optimization were an on-line approach and the application of a neural network. The on-line approach can be applied to an existing system to determine maximum capacity of the system at a given pressure drop or the minimum energy required for a given solids flow rate. A control algorithm uses

knowledge from the feedforward neural network and the performance index to produce the required gas flow rate such that the solids flow rate is maximized and the pressure drop across the system is at the maximum blower specifications. A simulation system for pneumatic conveying was developed by Mason et al. (1997) to help determine the optimal air supply needed for a particular system.

The energy for pneumatic conveyance of forage was characterized as energy for acceleration, impact and friction (Totten and Millier, 1966). The energy for accelerating the forage particles in a cut-and-blow forage harvester is provided by the blower. Past research into blower design has involved stationary forage blowers which can be applied to forage harvesters. Chancellor (1960) and Chancellor and Laduke (1960) investigated forage flow inside a stationary blower, up a vertical pipe and through a deflector elbow. It was estimated that in a 90° elbow, more than 50% of the kinetic energy of the forage was consumed by friction. Furthermore, it was found that more energy was lost by a particle hitting the elbow at some angle than by having the particle travel around the curved surface to an equivalent angle. For example, to change the direction of a particle by 45°, it would take less energy to have the particle impact a curved surface at 15° and travel around the curved surface another 30° than it would to simply impact a flat surface at 45°.

Research on the efficiency of spout design was conducted by Reznik (1966). It was determined that the design of the delivery spout was very important in conveying the chopped forage as efficiently as possible. The forage harvester used in Reznik's research

had an upward cutting cutterhead and a spout shape shown in Figure 2.2, where the forage was blown to the side.

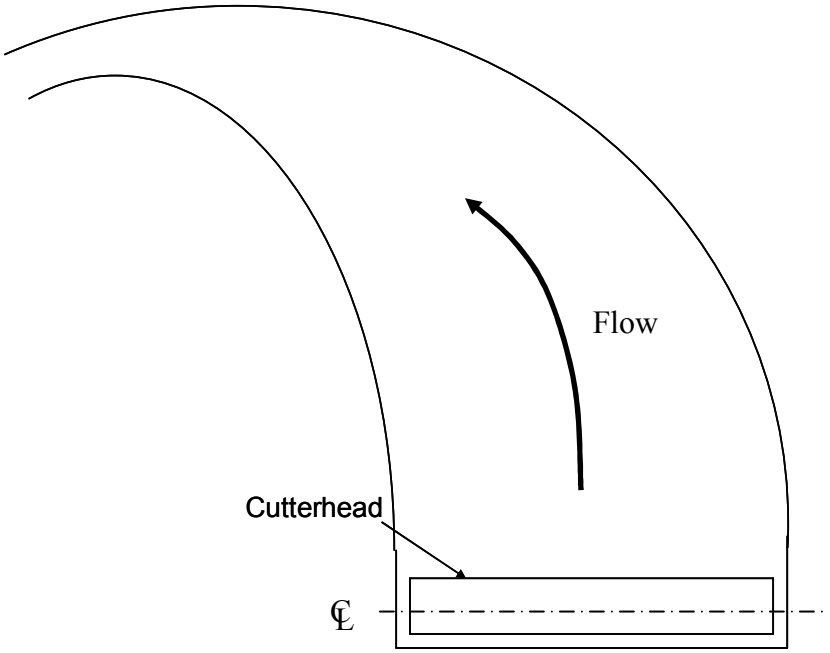

Figure 2.2 Spout shape used by Reznik (1966) as viewed from the rear of the forage harvester.

A transparent rear wall on the spout was used to observe the trajectory of forage pieces using high-speed photography. It was found that air currents in the spout contributed significantly to the motion of the forage and irregular air flow patterns caused loose forage streams and plugging in the spout. Air velocities at the spout exit for several cutterhead designs were measured with an air meter and it was found that velocity profiles with the greatest velocity at the top of the spout discharge opening were the most effective at conveying the forage.

3 OBJECTIVES

The general objectives of this project were to increase the throwing distance of a forage harvester and to develop a numerical model of the air flow using the computational fluid dynamics software, FLUENT. Specific objectives were:

1. to model the air flow through the fan and spout of a forage harvester and attempt to verify the model with experimental air flow measurements,
2. to model the flow of forage through the spout analytically with impact and friction models and
3. to optimize the path of forage particles in the spout with the analytical model and test two prototype spout designs relative to the current design.

4 AIR FLOW MODELING

4.1 Introduction

The fan in a forage harvester is used to convey chopped forage into a transport vehicle (either a truck or tow-behind wagon) so the forage can be removed from the field. The air flow provided by the fan helps the forage maintain velocity as it travels vertically through the collector and into the spout. Poor air flow patterns and vortices can affect the efficient flow of forage. Therefore the ability to model the air flow using a computer can be very beneficial, especially when evaluating new geometries or prototypes.

This Chapter will address the first objective stated in Chapter 3 beginning by declaring the coordinate system used throughout the thesis. The development of the numerical model will be outlined as well as the experimental procedure for the air flow measurements. The model output and experimental measurements will then be compared and discussed.

4.2 Coordinate System

The coordinate system for all measurements in this project (unless otherwise specified) placed the origin at the centre of the fan shaft and the inside surface on the right hand side of the fan housing as shown in Figure 4.1. The positive X direction is to the right of the machine, the positive Y direction to the front and the positive Z direction is straight up.

As well all references to the right or left sides of the forage harvester were determined by standing behind the machine and looking forward.

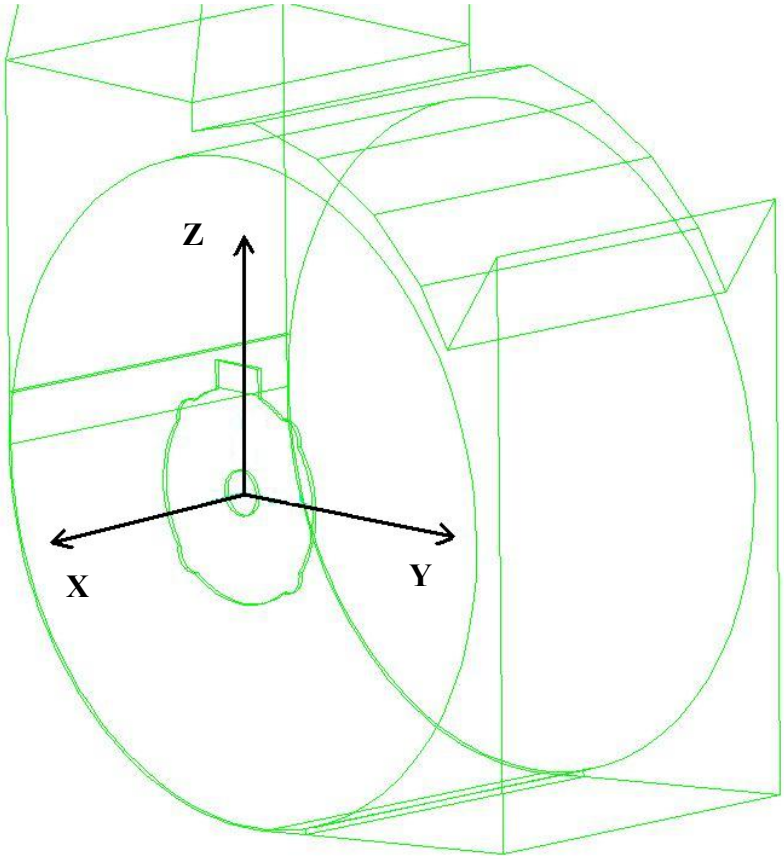

Figure 4.1 Coordinate system used throughout project locating origin and positive directions.

4.3 General Air Flow Directions

The general air flow in the fan, housing and collector model is shown in Figure 4.2 and in Figure 4.3 for the extension spout model. Air enters from in front of the fan and from each side through holes in the fan bearing holders. The air exits the fan in the vertical direction and then travels through the collector, extension and spout where it exits to the atmosphere.

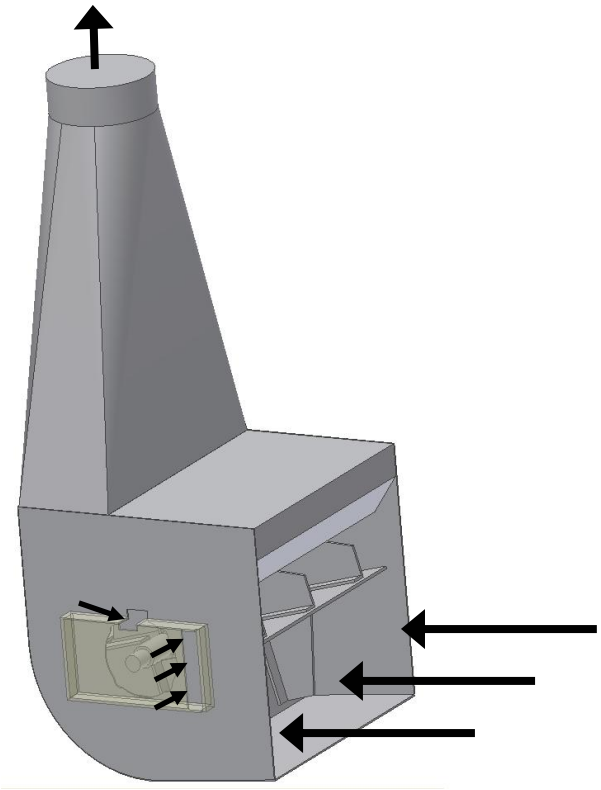

Figure 4.2 Air flow directions in the fan, housing and collector model.

Figure 4.3 Air flow directions in the extension and spout model.

4.4 Numerical Model

4.4.1 Background

To model the flow fluid in a domain requires solving the equations which describe that flow. These equations include the governing integral equations for the conservation of mass and momentum, and (when appropriate) for energy and other scalars such as turbulence and chemical species. In this project the conservation of energy is not included because heat transfer in the flow is not modeled; as well chemical species scalars are not applicable due to there not being any chemical reactions within the domain.

The equation for conservation of mass, sometimes referred to as the continuity equation, can be written as:

$$\frac{\partial \rho}{\partial t} + \nabla \cdot \left(\rho \vec{v} \right) = S_m , \tag{4.1}$$

where ρ = density,

t = time,

∇ = gradient,

$\vec{v}$ = velocity vector and

S_m = mass added to the continuous phase.

The equation the conservation of momentum in an inertial (non-accelerating) reference frame can be written as:

$$\frac{\partial}{\partial t}\left(\rho \vec{v}\right) + \nabla \cdot \left(\rho \vec{v} \vec{v}\right) = -\nabla p + \nabla \cdot \left(\bar{\bar{\tau}}\right) + \rho \vec{g} + \vec{F} , \tag{4.2}$$

where p = static pressure,

$\bar{\bar{\tau}}$ = stress tensor,

$\rho\vec{g}$ = gravitational body force and

$\vec{F}$ = external body forces.

The stress tensor can be described by:

$$\bar{\bar{\tau}} = \mu\left[\left(\nabla\vec{v} + \nabla\vec{v}^{T}\right)\right] - \frac{2}{3}\nabla\cdot\vec{v}I, \tag{4.3}$$

where μ = molecular viscosity,

I = unit tensor and

the second term on the right hand side is the effect of volume dilation.

FLUENT uses a control-volume-based technique to convert the governing equations to algebraic equations that can be solved numerically. This control volume technique consists of integrating the governing equations about each control volume, yielding discrete equations that conserve each quantity on a control-volume basis (FLUENT, 2003).

The governing equations can also be illustrated as the steady-state conservation equation for transport of a scalar quantity, ϕ, as shown by:

$$\underbrace{\frac{\partial}{\partial t}\int_{V}\rho\phi dV}_{\text{unsteady}} + \underbrace{\oint_{A}\rho\phi\vec{v}\cdot d\vec{A}}_{\text{convection}} = \underbrace{\oint_{A}\Gamma_{\phi}\nabla\phi\cdot d\vec{A}}_{\text{diffusion}} + \underbrace{\int_{V}S_{\phi}dV}_{\text{generation}}, \tag{4.4}$$

where $\vec{A}$ = surface area vector,

Γ_{ϕ} = diffusion coefficient for ϕ and

S_{ϕ} = source of ϕ per unit volume.

V = volume of control volume

For the continuity equation ϕ would be 1 and for the momentum equations ϕ would be *u, v* and *w* for the three directions *X*, *Y* and *Z* respectively. Each transport equation is then discretized into an algebraic form as shown by:

$$\frac{\left(\rho\phi_p\right)^{t+\Delta t} - \left(\rho\phi_p\right)^{t}}{\Delta t}\Delta V + \sum_{f}^{Nfaces} \rho_f \phi_f \vec{v}_f \cdot \vec{A}_f = \sum_{f}^{Nfaces} \Gamma_\phi \left(\nabla\phi\right)_n \cdot \vec{A}_f + S_\phi \nabla V \,, \qquad (4.5)$$

where *Nfaces* = number of faces enclosing control volume,

ϕ_f = value of ϕ convected through face *f*,

$\rho_f \vec{v}_f \cdot \vec{A}_f$ = mass flux through the face,

$\vec{A}_f$ = area of face *f*,

$\left(\nabla\phi\right)_n$ = magnitude of $\nabla\phi$ normal to face *f* and.

Each discretized transport equation is solved for every control volume in the domain.

For high Reynolds number flows, (> 3000) turbulence within the flow must be taken into account. Turbulence is the unsteady, irregular (aperiodic) motion in which transported quantities (mass, momentum and scalar species) fluctuate in time and space (FLUENT, 2005). In the extension spout model described below a Reynolds averaged approach is used to model the turbulent fluctuations. This approach introduces additional unknown variables into the governing equations. Therefore a turbulence model is used to produce a closed set of equations. A more in depth explanation of turbulence modeling can be found in FLUENT (2003).

4.4.2 Development steps

The overall objective of the numerical model was to utilize CFD software (FLUENT 6.1, FLUENT Inc., Lebanon, NH) to simulate the air flow patterns and velocities in the fan and spout of the forage harvester. The steps followed to achieve this objective were to:

1. develop a solid model of the flow domain using solid modeling software,
2. mesh the solid model in Gambit (CFD preprocessor) and
3. perform simulations using FLUENT.

4.4.3 Flow domain

The flow domain used in the computer model consisted of the fan, fan housing, collector, extension, spout and the domain extension as shown in Figure 4.4. The domain extension was added to the spout to reduce back flow into the domain due to the open area at the bottom of the spout at the end as shown in Figure 4.3.

4.4.4 Models

Due to the location of the inlets and outlets a two-dimensional model would not accurately describe the flow patterns. Therefore a three-dimensional model needed to be created.

To develop the flow domain two-dimensional drawings of the blower and spout were used to create a three-dimensional model. Two-dimensional drawings of a Dion 1224 pull-type forage harvester were supplied by Dion Machineries Inc. and imported into Autodesk Inventor 6, a three-dimensional solid modeling software package. Separate parts were created for each solid piece within the flow domain. These parts were then assembled together to complete the three-dimensional model.

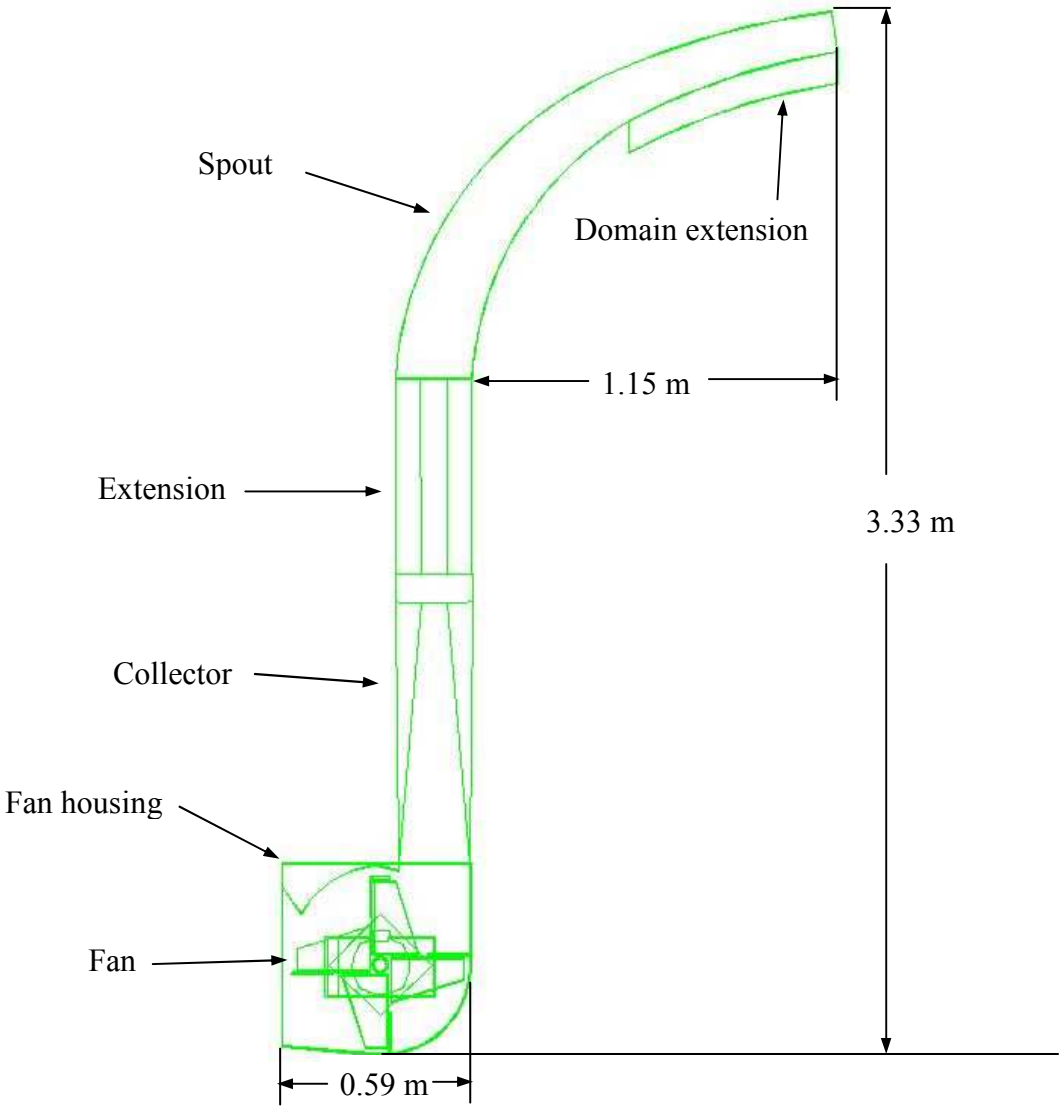

Figure 4.4 Flow domain used in numerical model with major dimensions.

All surfaces within the models were modeled as being smooth. This is different from the actual machine due to roughness of the different surfaces such as metal, paint and build up from high moisture crops, for example corn. Fasteners used to connect the different parts were not included in the model. As well the model did not account for any leakage between joints.

The solid model was then imported into Gambit, a CFD pre-processor where meshing was performed and boundary conditions were applied. The extension and parts of the spout were created in Gambit. To reduce the simulation times the fan, housing and collector model were split exactly in half as shown in Figure 4.5.

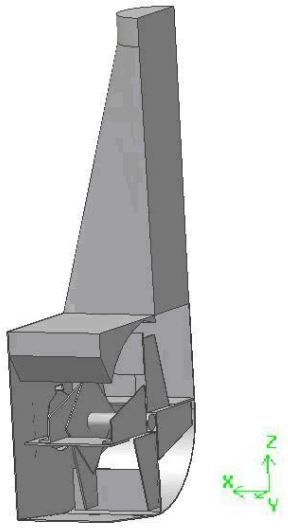

Figure 4.5 Half section of fan, housing and collector model.

The simulations were completed in two stages: the first being the fan, housing and collector ending where the collector attaches to the extension, and the second consisted of the 0.61-m (2-ft) spout extension and spout. Initially the collector was to be included with the spout and extension but was moved to the fan and housing to eliminate backflow at the housing and collector interface.

4.4.5 Meshing

4.4.5.1 Fan, housing and collector

The meshing of the fan, housing and collector model was divided into five volumes. The volumes include the bearing holder (Figure 4.6), fan shaft hole (Figure 4.7), moving fan (Figure 4.8), main housing (Figure 4.9) and the collector (Figure 4.10).

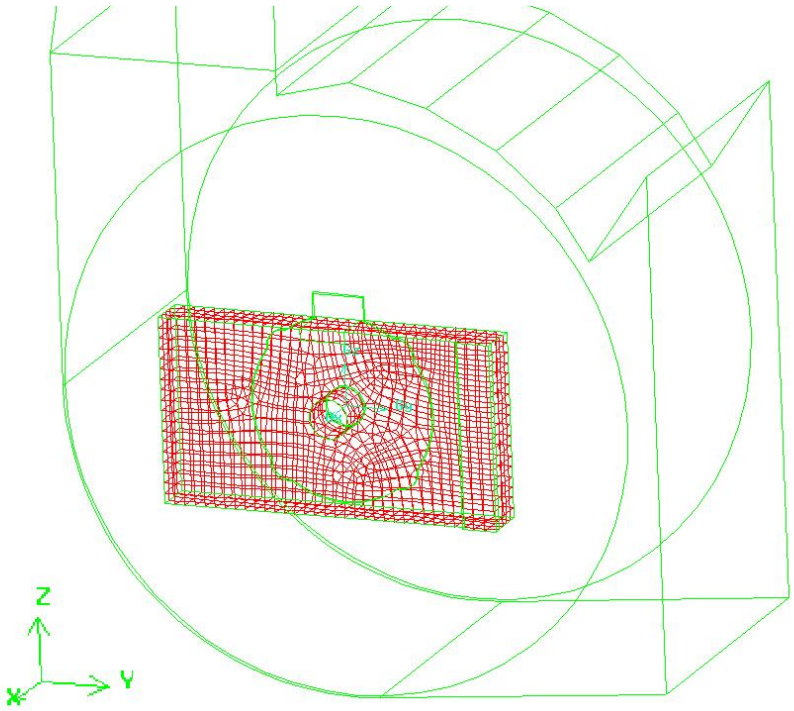

Figure 4.6 View of mesh used on bearing holder.

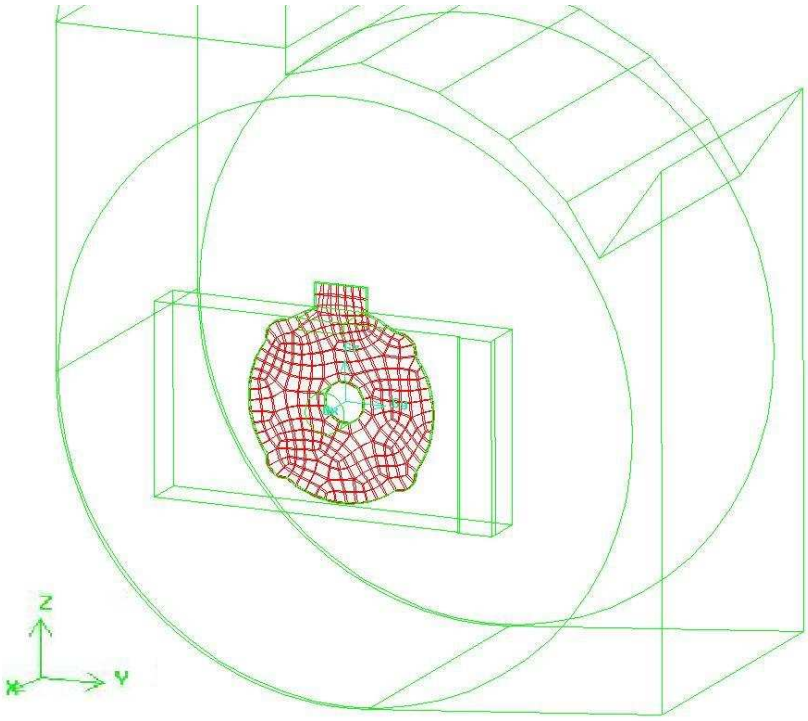

Figure 4.7 View of mesh used on fan shaft hole.

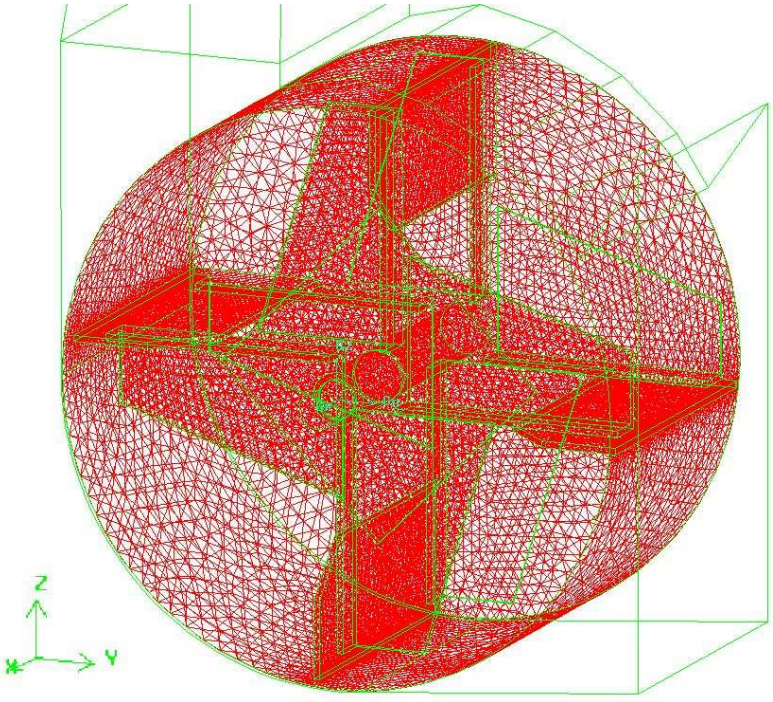

Figure 4.8 View of mesh used on moving fan.

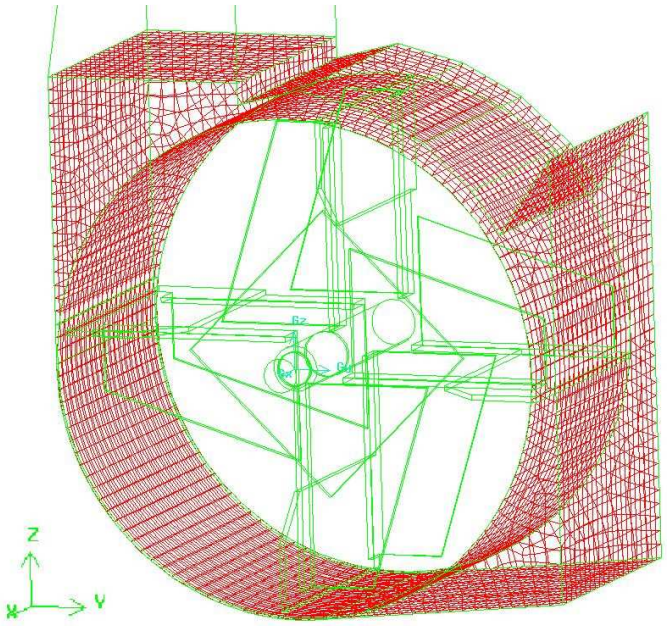

Figure 4.9 View of mesh used on main housing.

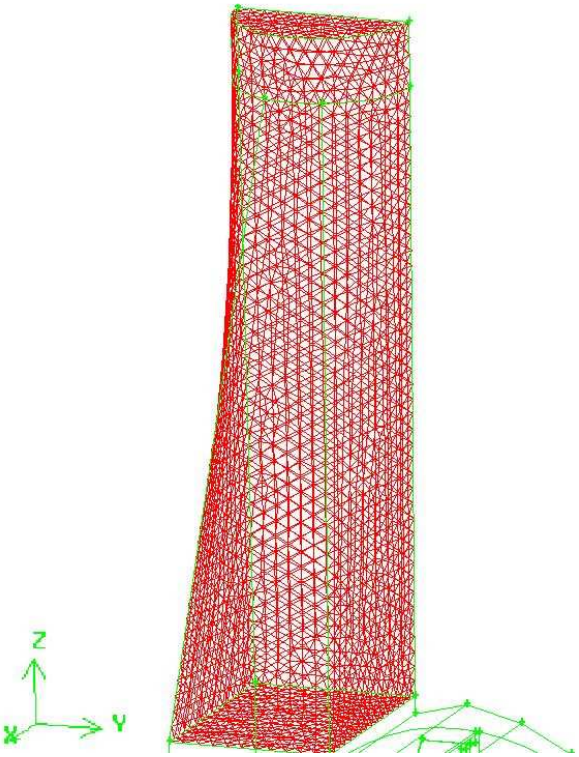

Figure 4.10 View of mesh used on collector.

Two methods were used to mesh the five volumes of the fan, housing and collector model. The first was a Cooper scheme which treats the volume as consisting of one or more logical cylinders composed of two end caps and a barrel. The two end caps are called source faces and the barrels are non-source faces. Gambit then automatically performs the following operations on the volume.

1. Mesh the non-source faces (Figure 4.11(a)).
2. Imprint the source faces onto each other (Figure 4.11(b)). (NOTE: Regions *A'* and *B'* represent the imprinting of faces *A* and *B*, respectively.)
3. Mesh each of the source faces (Figure 4.11(c)).
4. Project the source-face mesh node patterns through the volume (Figure 4.11(d)).

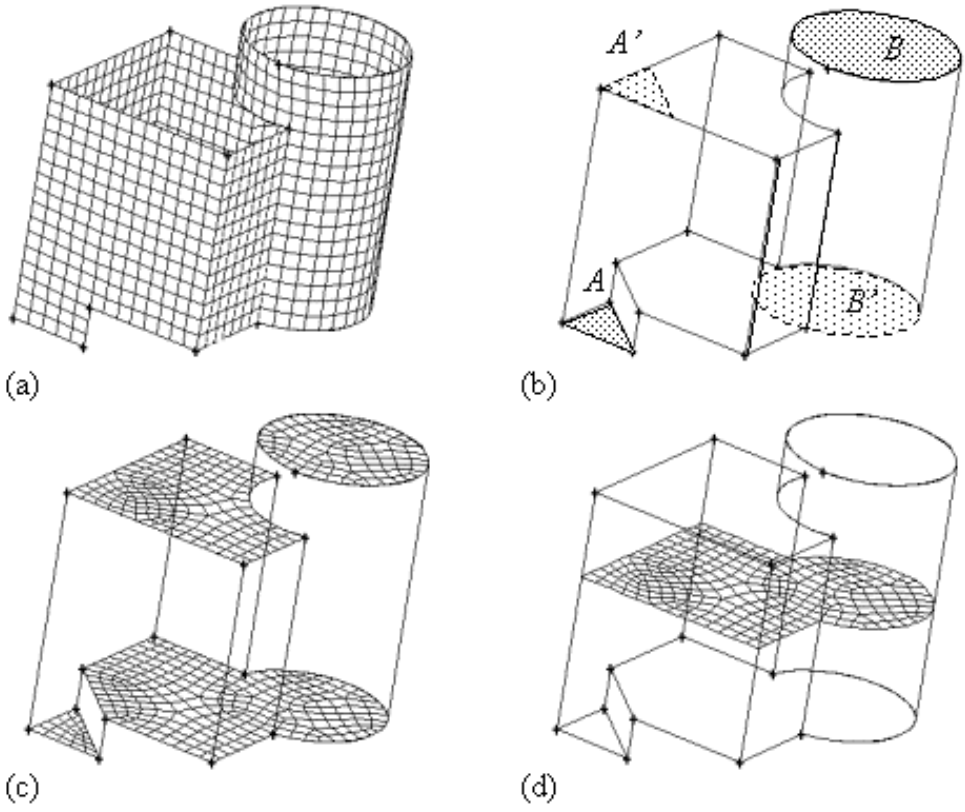

Figure 4.11 Example of Cooper volume meshing scheme (Gambit, 2003).

The second method used for meshing was a TGrid meshing scheme. This method creates a mesh that consists primarily of tetrahedral mesh elements but which may also contain elements that possess other shapes. The quality of the meshes was evaluated by examining the EquiAngle Skew of the elements which is a normalized measure of the skewness of each element. The measure ranges from 0 (perfect element) to 1 (degenerate element). Table 4.1 lists the specifications for each of the volume meshes.

Table 4.1: Details of meshing for the five volumes of the fan, housing and collector model.

	Mesh Scheme	# of Elements	Worst EquiAngle Skew
Bearing Holder	Cooper	2390	0.515
Fan Shaft Hole	Cooper	288	0.536
Moving Fan	TGrid	275771	0.861
Main Housing	Cooper	6279	0.492
Collector	TGrid	31562	0.802

The five volume meshes are combined using the FLUENT utility tmerge to create a single mesh file with a non-conformal grid. A non-conformal grid is composed of cell zones where the grid node locations do not need to be identical at the boundaries where two subdomains meet.

4.4.5.2 Extension and spout

The meshing of the extension and spout model was divided into two volumes. The volumes include the extension (Figure 4.12), and the spout (Figure 4.13). The two meshes were combined in the same way as described for the fan, housing and collector model. Table 4.2 lists the specifications for the extension and spout meshes.

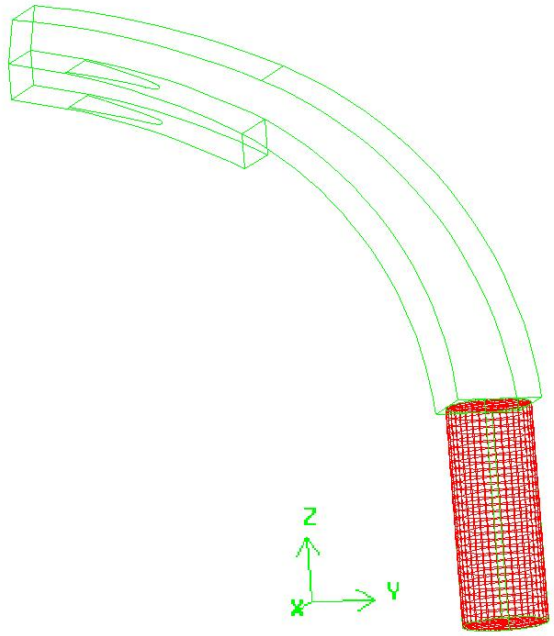

Figure 4.12 View of mesh used on the extension.

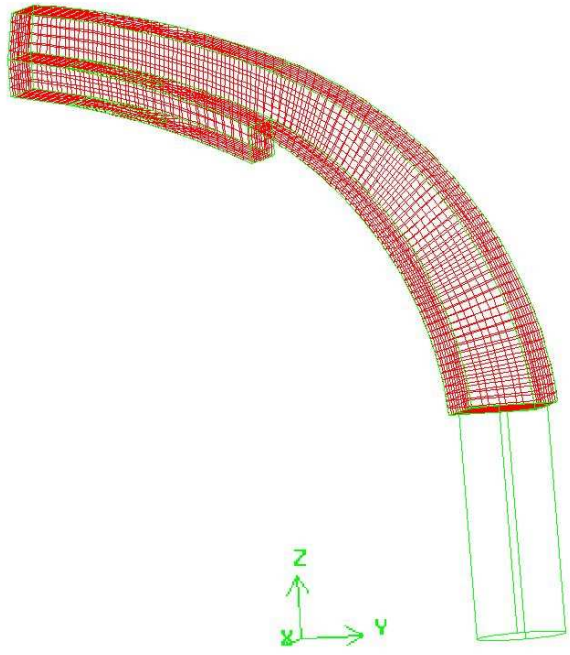

Figure 4.13 View of mesh used on the spout.

Table 4.2: Details of meshing for the two volumes of the extension and spout model.

	Mesh Scheme	# of Elements	Worst EquiAngle Skew
Extension	Cooper	4185	0.733
Spout	Cooper	4890	0.459

4.4.6 Boundary conditions

The fluid used in both models was air with a density of 1.225 kg/m^3 and viscosity of 1.7894 x 10^{-5} kg/ms

4.4.6.1 Fan, housing and collector

There were seven boundary faces, faces where air either entered or left the domain, used on the fan, housing and collector. There were five pressure inlets located at the bearing holder (Figure 4.14) and two pressure outlets located at the collector outlet and at the front face of the housing (Figure 4.15).

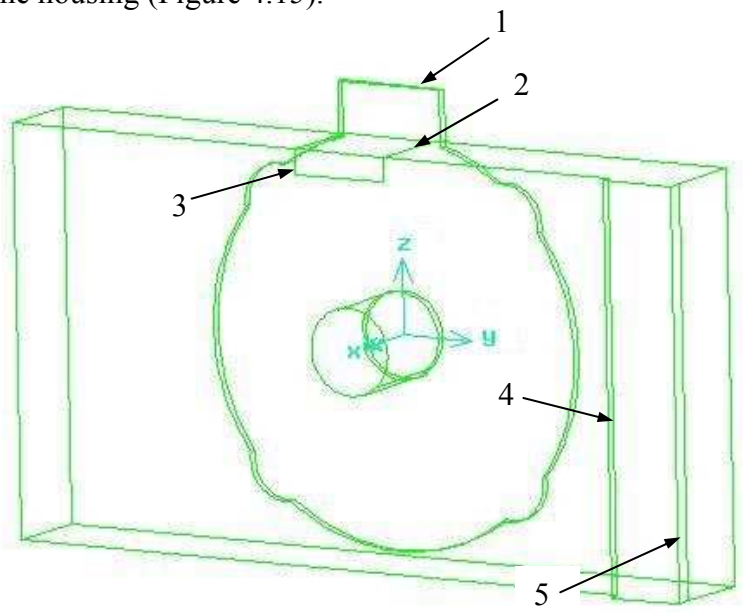

Figure 4.14 Pressure inlet boundary conditions numbered 1 to 5 for the fan, housing and collector flow domain.

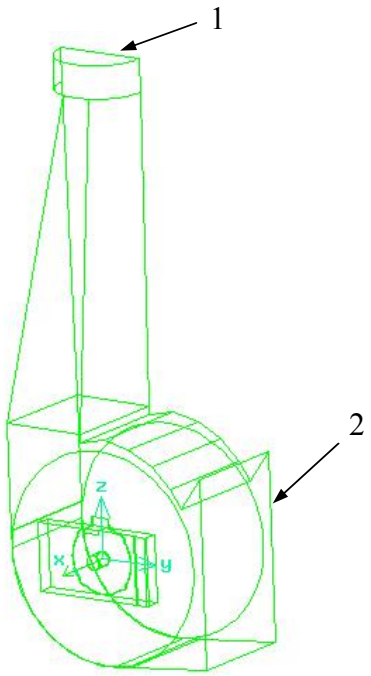

Figure 4.15 Pressure outlet boundary conditions numbered 1 and 2 for the fan, housing and collector flow domain.

From initial simulations it was found that the overall flow at pressure outlet 2 was into the domain but there was also certain points where there was air moving out of the domain. Therefore a pressure outlet boundary condition (BC) was used because the pressure outlet BC in FLUENT has reverse flow settings that the pressure inlet BC does not. For the simulation all the boundary conditions were initially set to 0 Pa gauge pressure or equal to atmospheric pressure. After simulation of the extension spout model, pressure outlet 1 was set to 130 Pa which was the static pressure at that boundary predicted by the extension spout simulation.

To simulate the rotational movement of the fan the flow domain inside the housing was split in two sections by a sliding boundary around the fan blades as shown in Figure 4.16 that has the fan removed. The fan blades and the mesh surrounding them out to the sliding boundary had a rotational boundary condition of 1440 rpm to simulate the movement of the fan.

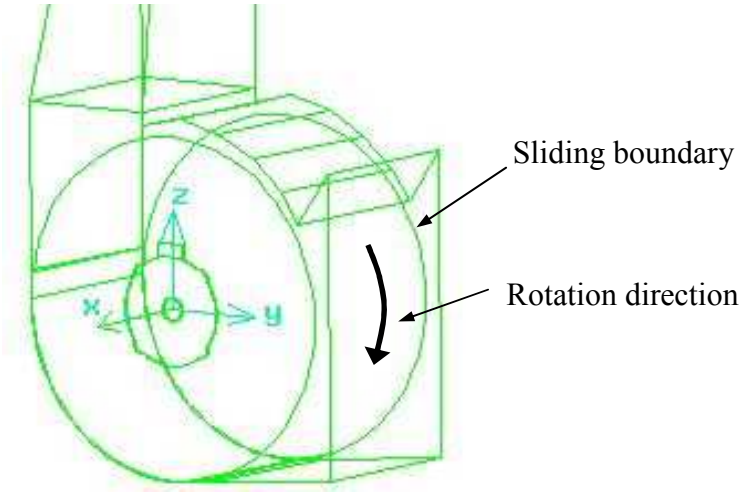

Figure 4.16 Sliding boundary around the fan blades of the fan, housing and collector model.

4.4.6.2 Extension and spout

The boundary conditions used on the spout portion were a velocity inlet at the beginning of the collector and two pressure outlets at the end of the spout shown in Figure 4.17 (in which the picture was rotated to better view the boundaries). The second pressure outlet was required due to the extra flow area added to reduce the amount of back flow that occurred along the open area at the end of the spout.

The velocity inlet was set to 15 m/s, which was the average of the measured velocities at zone 4. The two pressure outlets were set to 0 Pa gauge pressure.

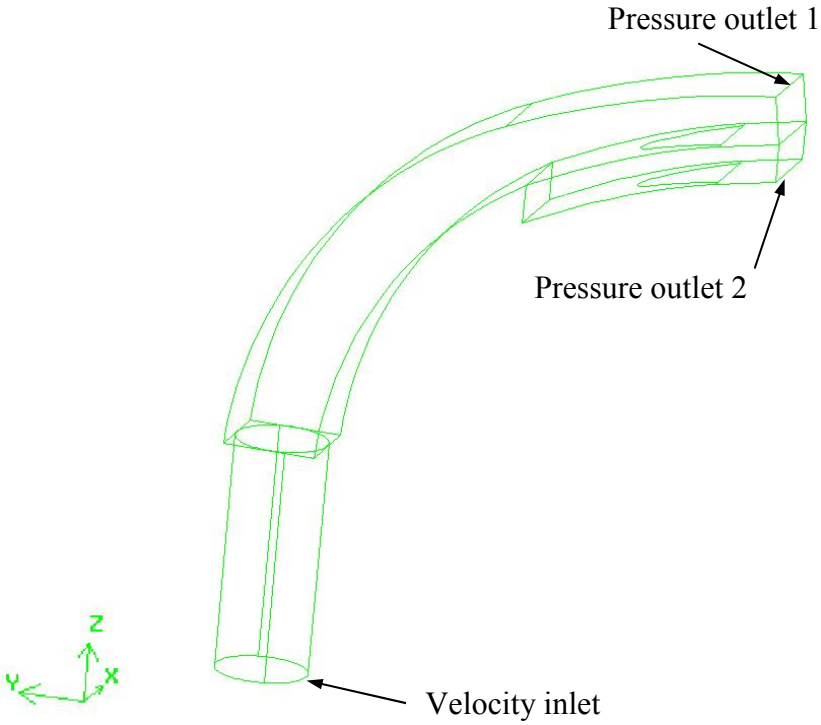

Figure 4.17 Boundary conditions for the extension and spout flow domain.

4.4.7 Solution procedure

After meshing was completed and the boundary conditions were set, the mesh was imported into FLUENT where simulations were executed. The simulations for the two models required different procedures which will be described in the next two sections.

4.4.7.1 Fan, housing and collector

The procedure for executing a simulation of the fan portion consisted of 500 iterations using the steady state multiple reference frame method. The model was then switched to an unsteady configuration using the sliding mesh method and executed for 5 revolutions of the fan using a 1st-order implicit unsteady formulation. The unsteady formulation was

then changed to 2nd-order implicit, which provided improved accuracy (FLUENT, 2003), and the model was executed for 16 revolutions.

The discretization scheme for momentum was changed to 2nd-order upwind. A 2nd-order scheme is recommended when the flow is not aligned with the grid (FLUENT, 2003), as is the case when using a tetrahedral grid like that used on the collector and the fan. A stable flow could not be achieved using the 2nd-order scheme therefore the data from the 1st-order discretization scheme were used in the results. The discretization schemes used for pressure interpolation and pressure-velocity coupling was PRESTO! and PISO respectively.

The air flow inside the fan, housing collector model was a turbulent flow. But due to the high computational requirements and complexity of the model, a turbulence model was not used.

Convergence of the model was monitored by plotting the mass flow rate at the collector outlet. When this value reached a periodic steady state the flow was assumed to have converged. Periodic steady state was determined by plotting the mass flow rate versus the simulation time. Figure 4.18 shows an example of the mass flow rate from the collector outlet. The plot shows the solution procedure where at 0.219 s the solver was changed to 2nd-order implicit and at 0.636 s the 2nd-order upwind discretization scheme for momentum was selected after which the mass flow rate did not reach a periodic steady state.

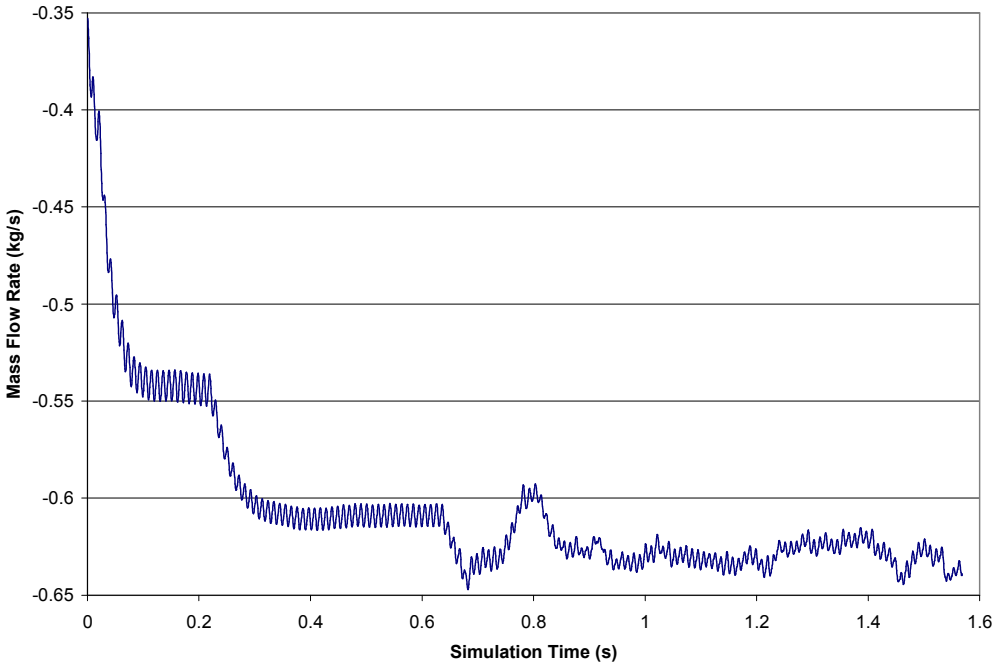

Figure 4.18 Example plot of mass flow rate at collector outlet.

The mass flow rate balance at all inlets and outlets was also calculated to ensure that the mass imbalance was less than 0.1% of the total flow as recommended by FLUENT (2003). When convergence was achieved data sampling for time statistics was turned on for one complete rotation which provided the averages of all values for as long as it was turned on. This provided the average velocity coming from the fan, which was equivalent to what was measured with the anemometer due to the fact that the anemometer data were also averaged.

4.4.7.2 Extension and spout

The procedure for executing a simulation of flow through the extension and spout was started by having the flow converge without a turbulence model selected. The flow in the spout had an average Reynolds number of approximately 230,000 using the diameter of

the extension as the length scale, which is well into the turbulent region. Therefore a turbulence model was added to the simulation. The standard k-ε turbulence model was chosen due to its robustness, economy, and reasonable accuracy for a wide range of turbulent flows (FLUENT, 2003). This model introduces two new equations which model the turbulence kinetic energy, k, and its rate of dissipation, ε. The default values for the model constants were used and are given in Table 4.3.

Table 4.3: Constants in k-ε model.

$C_{1\varepsilon}$	1.44
$C_{2\varepsilon}$	1.92
C_{μ}	0.09
σ_k	1.0
σ_{ε}	1.3

Then a 2nd-order upwind discretization scheme for momentum was added and the model was executed until convergence. The standard discretization scheme was used for pressure interpolation and the SIMPLE scheme was used for pressure-velocity coupling. Also a 2nd-order upwind discretization scheme was used for the turbulent kinetic energy and dissipation rate. Finally the grid was adapted to ensure compatibility with the standard wall functions used with the k-ε turbulence model. Wall functions are used to bridge the viscosity-affected region between the wall and the fully-turbulent region because turbulent flows are significantly affected by the presence of walls.

Convergence was determined by the residuals which are the imbalance of the conservation equation summed over all the computational cells (FLUENT, 2003). For each simulation the model was iterated until the residuals were reduced to less than 1.0 x

10^{-6} (Figure 4.19). As with the fan, housing and collector the mass flow rate imbalance was also monitored to ensure it was within 0.1 % of the total mass flow rate.

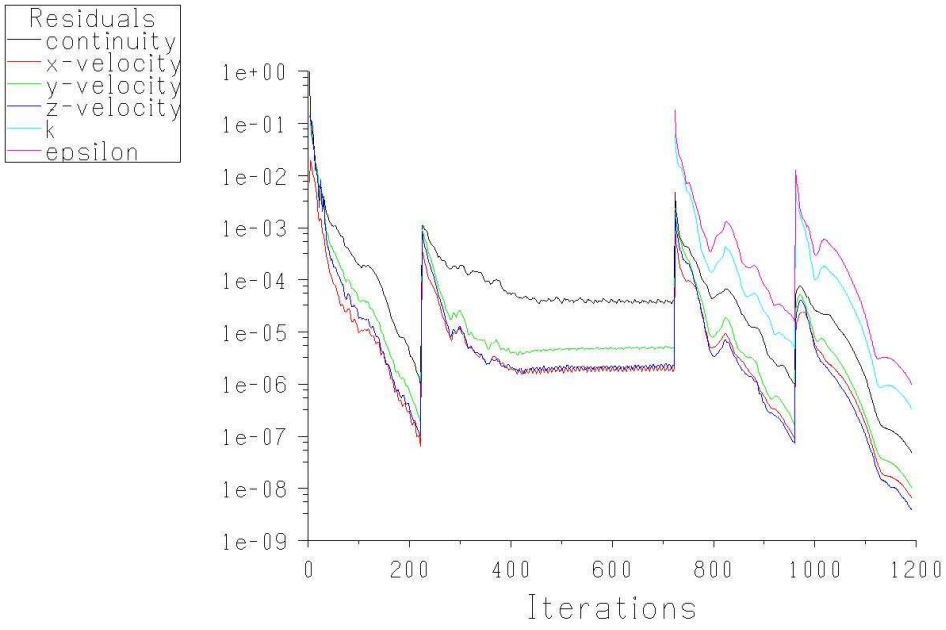

Figure 4.19 Plot of residuals from CFD simulation of extension and spout.

4.4.8 Grid refinement

4.4.8.1 Fan, housing and collector

Grid refinement was completed using the adaption function in FLUENT. This function allows more cells to be added in the grid where they are needed most based on the solution already obtained for the flow. In this model a gradient approach was used that increased the number of cells in areas where the gradient of velocity magnitude was high. The number of cells was increased from 316,290 to 362,130. The mass flow rate at the collector outlet was 0.493 kg/s for the original mesh and 0.501 kg/s for the refined mesh. This shows that the flow was increased by only 1.6 % and therefore the original mesh should be accurate enough given the added simulation time required for the larger mesh.

4.4.8.2 Extension and spout

The extension and spout model grid was also refined using the adaption function in FLUENT. The first adaption was made based on the y^+ value so that the grid was compatible with the standard wall functions used with the turbulence model. The second and third adaption used the gradient of velocity magnitude and were completed to accurately capture at line H (described in the next section). Figure 4.20 shows the plot of velocity magnitude for each adaption with the final one showing the symmetrical flow pattern.

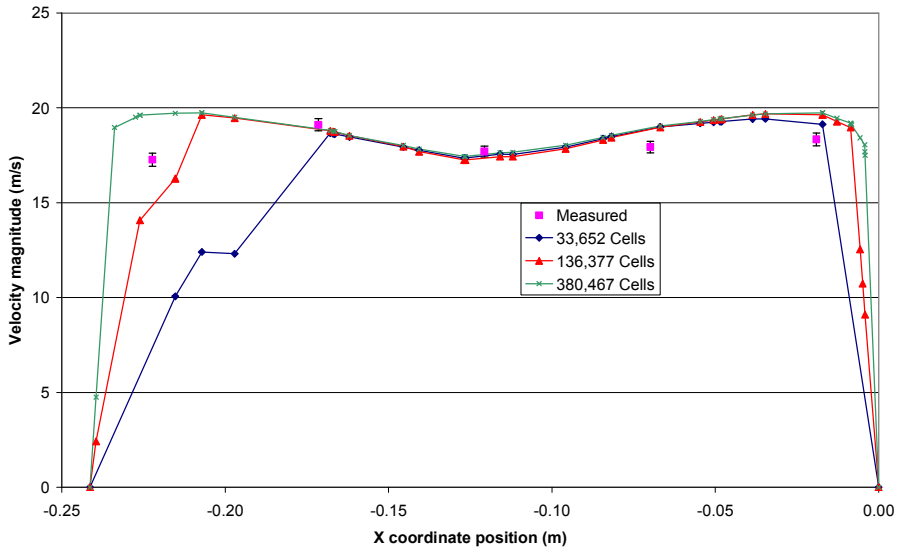

Figure 4.20 Measured and grid refined velocity magnitudes at line H of zone 5 using the origin shown in Figure 4.29.

4.5 Air Flow Measurement

The development of a numerical model of the air flow in the blower and the spout required boundary conditions for input into the model and verification of the predicted

output. Therefore measurements of the air flow were performed at several places on a forage harvester.

4.5.1 Materials and methods

Air flow measurements were performed on a Dion 1224 pull-type forage harvester. The harvester remained stationary during the tests and no crop was fed into the machine. Air velocity measurements were completed using a TSI model 8450 hot film anemometer with a measurement range of 0 to 50 m/s. The anemometer was calibrated in a TSI model 8390 bench-top wind tunnel in the 0 to 40 m/s range.

Figure 4.21 TSI model 8450 hot film anemometer.

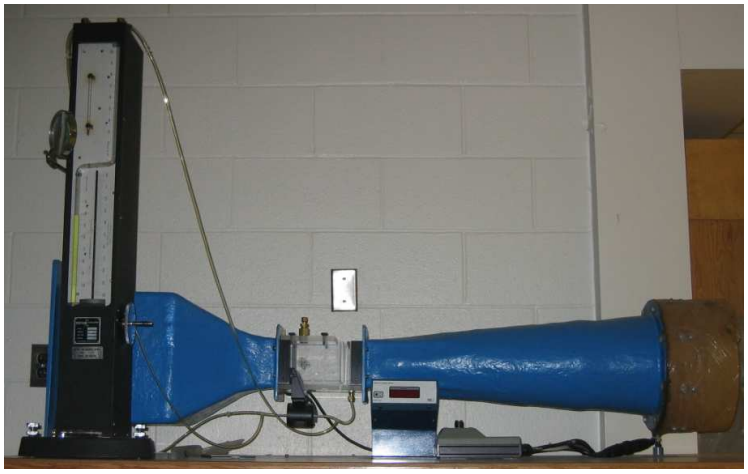

Figure 4.22 TSI model 8390 bench-top wind tunnel.

Measurements were taken within several planes on the harvester as shown in Figures 4.23 and 4.24. Zone 1 was a vertical plane at Y = 0.31 m in between the fan and the cutterhead. Zone 2 was the two openings on the bearing holder with the top opening at X = 0.004 m and the side opening on a plane at X = 0.05 m. Zone 3 was the horizontal plane at Z = 0.32 m where the collector attached to the fan housing. Zone 4 was the horizontal plane where the extension attached to the collector at Z = 1.23 m and zone 5 was a plane perpendicular to the bottom curvature of the spout at 0.419 m as measured from the end of the spout.

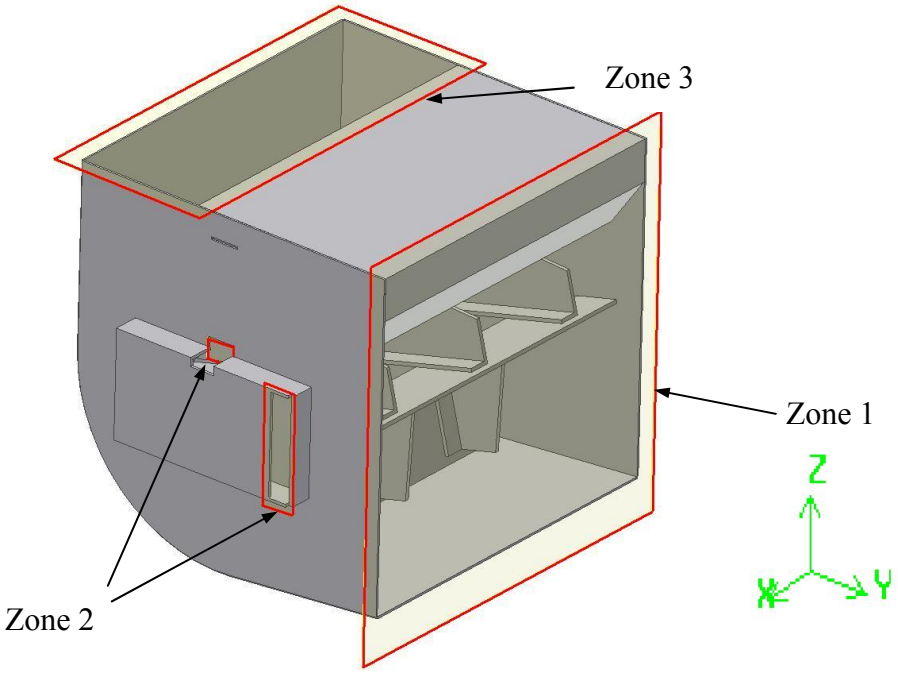

Figure 4.23 Planes of velocity measurements on the fan and housing – zones 1 to 3.

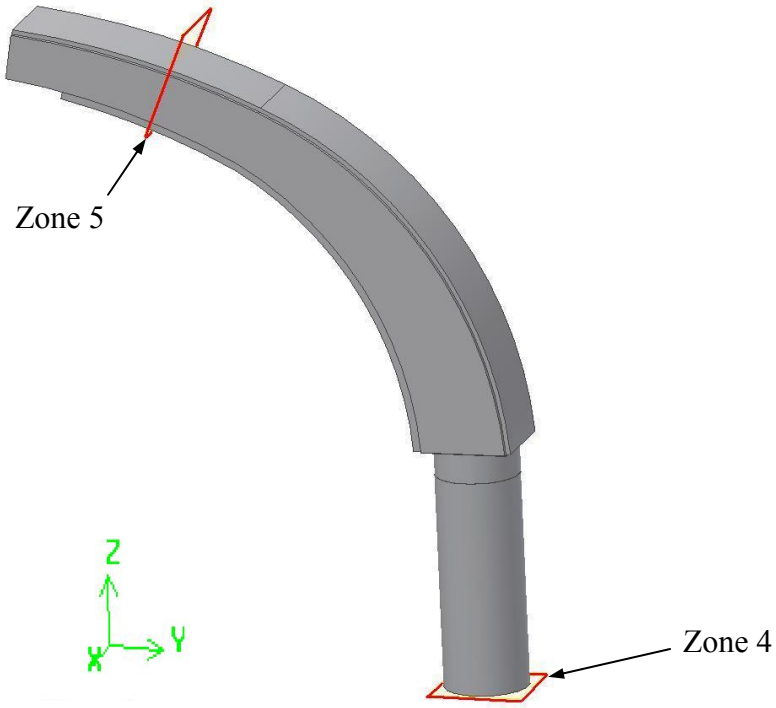

Figure 4.24 Planes of velocity measurements on the extension and spout – zones 4 and 5.

Initial measurements with the anemometer were made using a multimeter to measure the voltages that were then recorded manually. This method was used for zones one and two. Three repeated measurements were recorded, and the average and standard deviation were calculated. The standard deviation was found to be in the range of 1 to 2 m/s, so for the rest of the air measurements a Measurement Computing PPIO-AI08 12-Bit data logger was utilized to record the voltages. The data logger program was written in QuickBasic and was setup to log voltages for 5 seconds at 1000 Hz. The average and standard deviation were then calculated for each measurement position.

The measurement positions for each zone are shown in Figures 4.25 through 4.29. The positions were chosen by using existing holes in the harvester or by attempting to get an even distribution across the measurement plane. The depth of the probe in each hole was determined by marks on the probe body. Also the probe was rotated such that it was

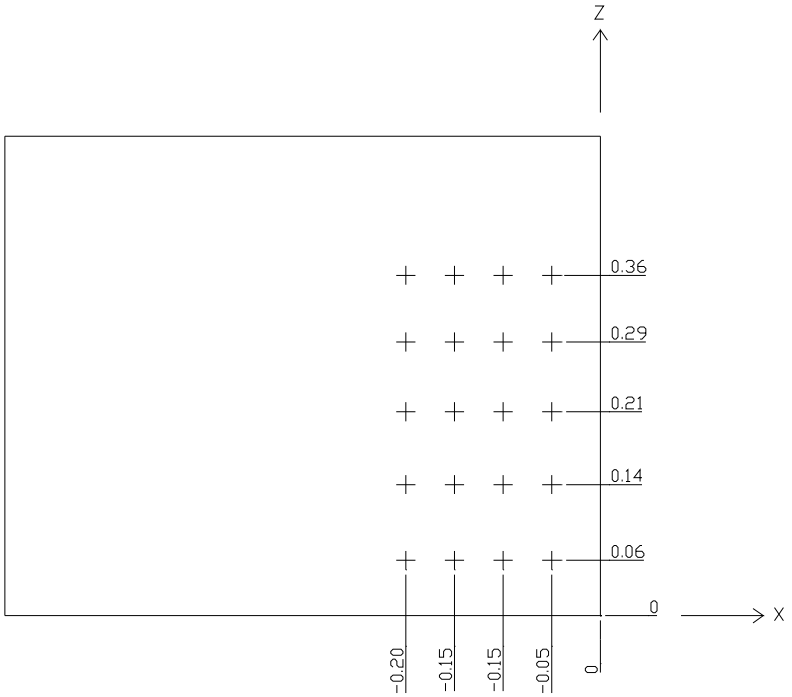

Figure 4.25 Velocity measurement positions (m) for zone 1 as measured from the origin shown.

perpendicular to the measurement plane. Only the right half of zone one was measured due to the limitation in the length of the hot film anemometer. Also it was unsafe to take measurements from the left side due to the presence of the fan drive belt.

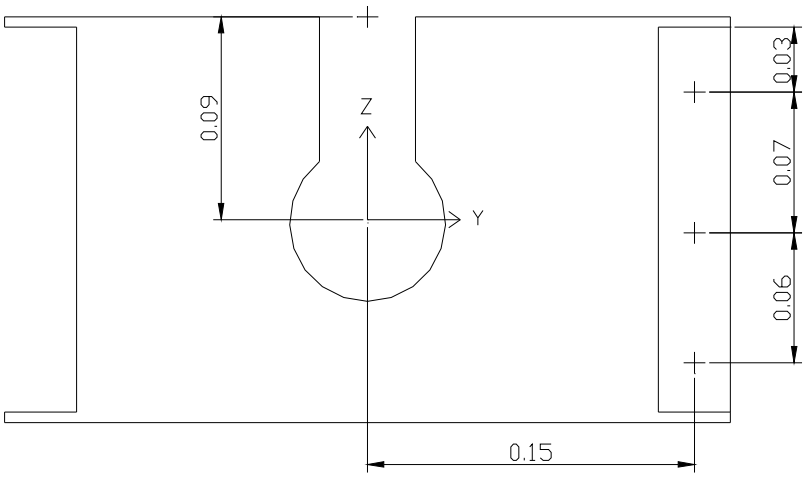

Figure 4.26 Velocity measurement positions (m) for zone 2.

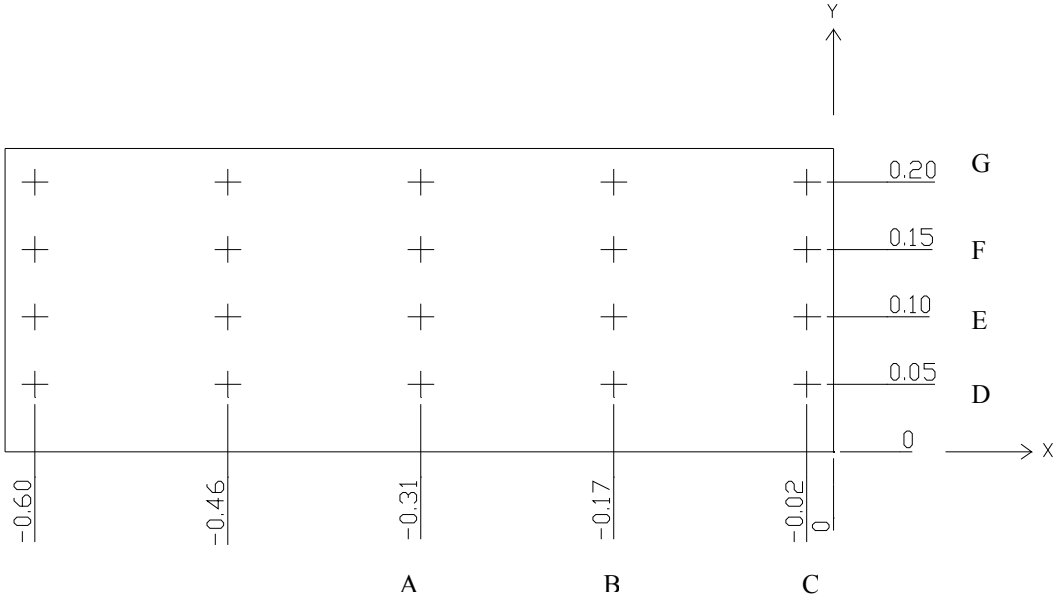

Figure 4.27 Velocity measurement positions (m) for zone 3 as measured from the origin shown.

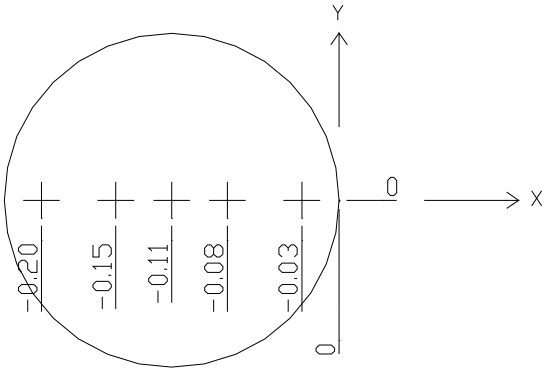

Figure 4.28 Velocity measurement positions (m) for zone 4 as measured from the origin shown.

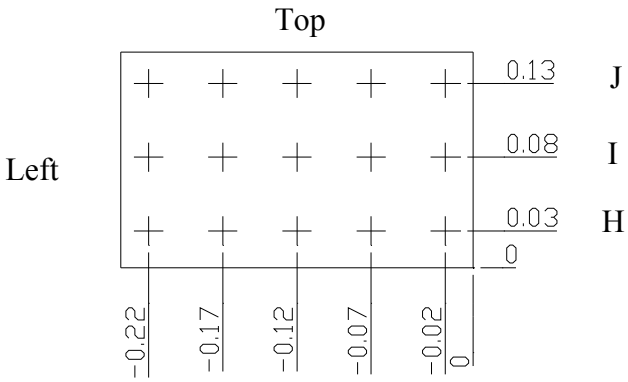

Figure 4.29 Velocity measurement positions (m) for zone 5 as measured from the origin shown.

4.5.2 Results

From the velocity measurements it was found that the air moving through zone 3 ranged from approximately 5 to 15 m/s. The velocities on the left side tended to be lower than the right side likely due to the fan drive pulley restricting air flow. The velocities at the front of the zone were lower than the rear. It should also be noted that the anemometer only measured velocity perpendicular to the measurement plane and could not distinguish

between flow in the positive or negative Z direction. Air velocity through zone 4 averaged 15 m/s and through zone 5 ranged from 17 to 19 m/s.

The results of the average velocity measurements for each position are given in Appendix A along with their standard deviations. Further comments on the experimental data are contained in the following section where it is compared to the output of the numerical model.

4.6 Validation

4.6.1 Fan, housing and collector

To get an idea of the flow patterns within the blower, several 2-D vector plots were produced from the simulation. When modeling in three dimensions it was difficult to visualize what was happening "inside" the model. To overcome this problem planes were created that showed all the vectors within the flow domain relative to one coordinate direction. Figure 4.30 shows the position of the plane perpendicular to the Y direction and Figure 4.31 shows the position of the planes perpendicular to the X direction

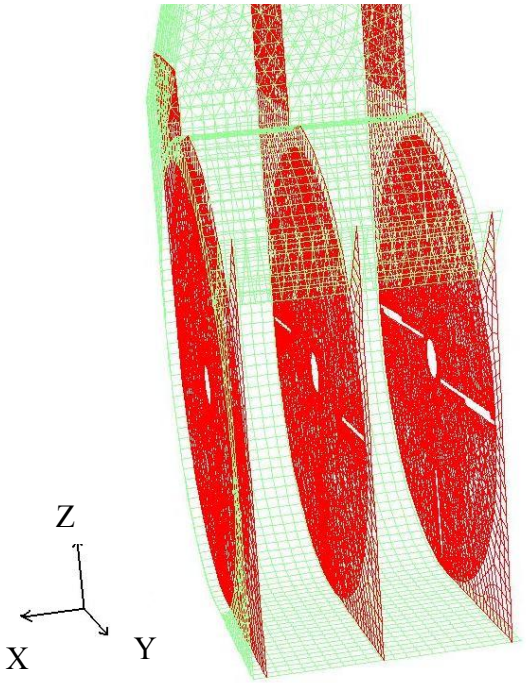

Figure 4.31 Vector planes positioned at X = -0.015, -0.15 and -0.3 m in the fan, housing and collector model.

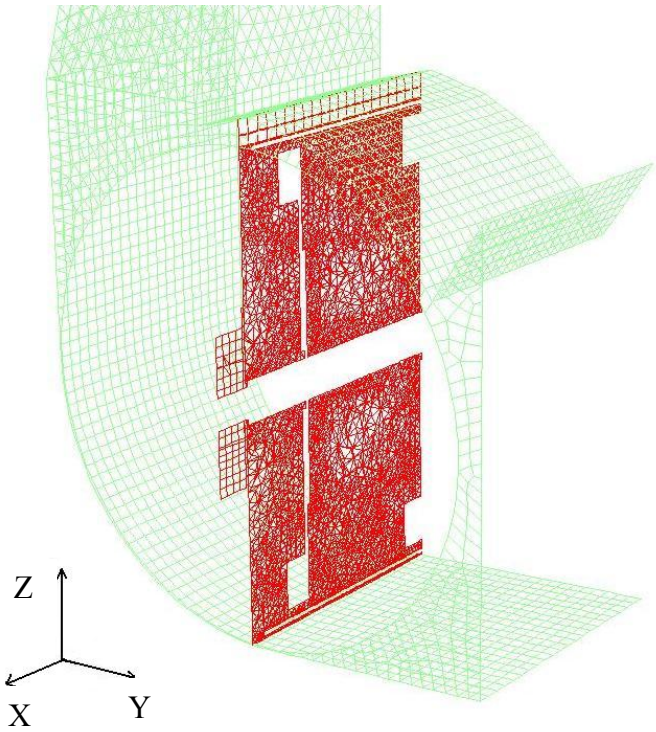

Figure 4.30 Vector plane positioned at Y = 0 m in the fan, housing and collector model.

The planes perpendicular to the X direction were positioned at X = -0.015, -0.15 and -0.3 m as measured from the origin described in Section 4.2. The plane perpendicular to the Y direction was positioned at Y = 0 m measured from the same origin.

The following figures show the vector plots for the aforementioned planes. The vector plot at X = 0.015 m (Figure 4.32) is located between the housing wall and the fan blade. A vortex can be seen above (positive Z direction) and to the left (negative Y direction) of the fan shaft which is due to the incoming air from the bearing inlets as can be seen in Figure 4.36. Figure 4.33 is an enlarged view of the square in Figure 4.32 that shows the vortex and the flow in the negative Z direction at the front of the collector. Figures 4.34 and 4.35 show a more uniform flow with less reverse flow at the front of the collector. The reverse flow is one place where the fan could be improved. If the reverse flow could be reduced then air flow into the spout would increase.

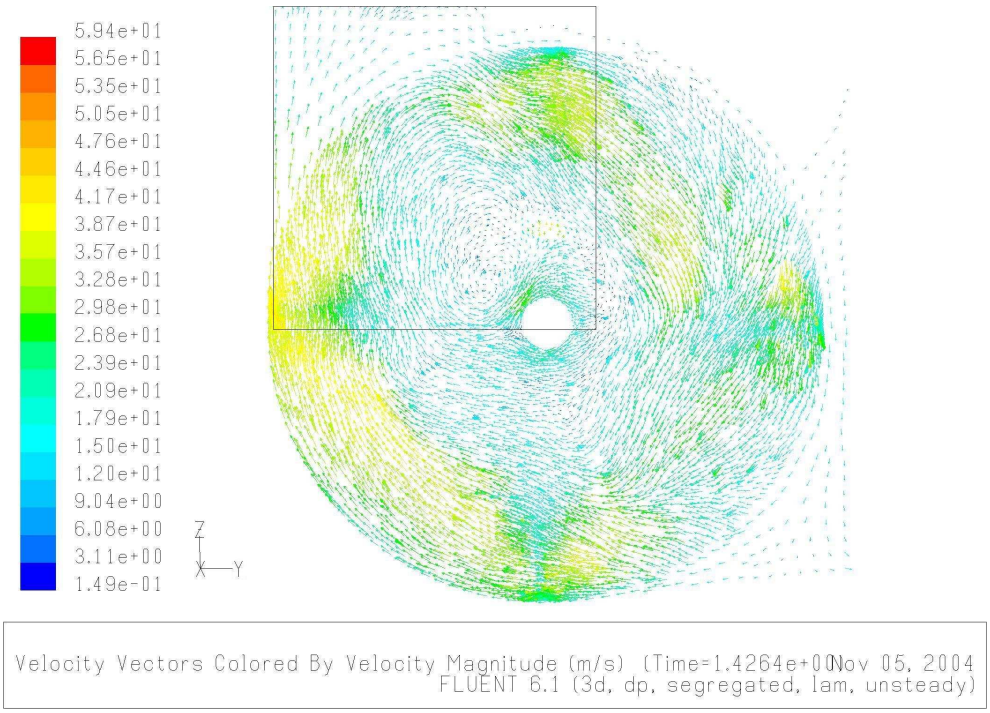

Figure 4.32 Vector plot at plane position X = -0.015 m (m/s).

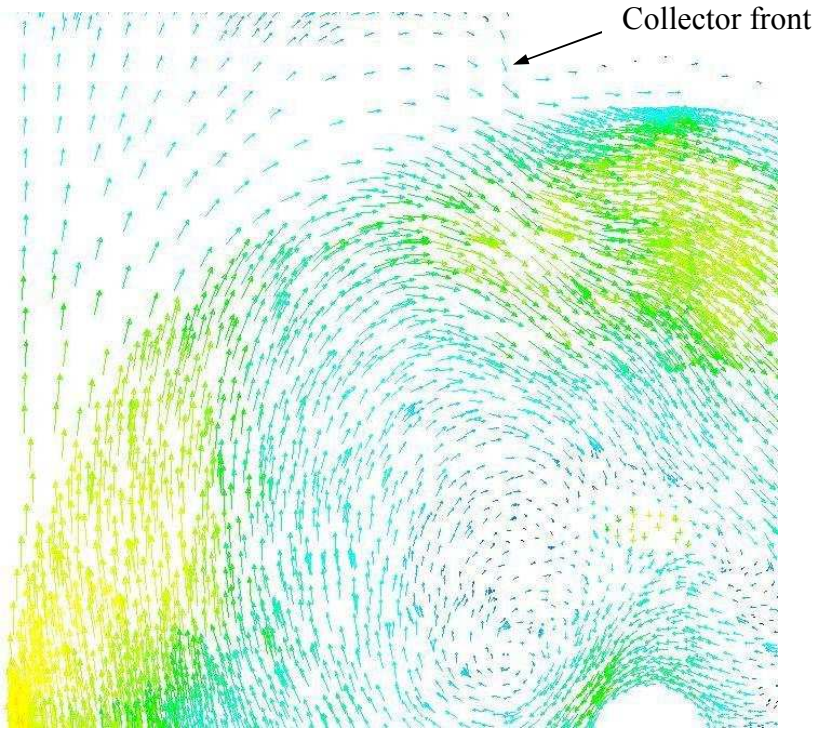

Figure 4.33 Close up of vortex from vector plot at plane position X = -0.015 m.

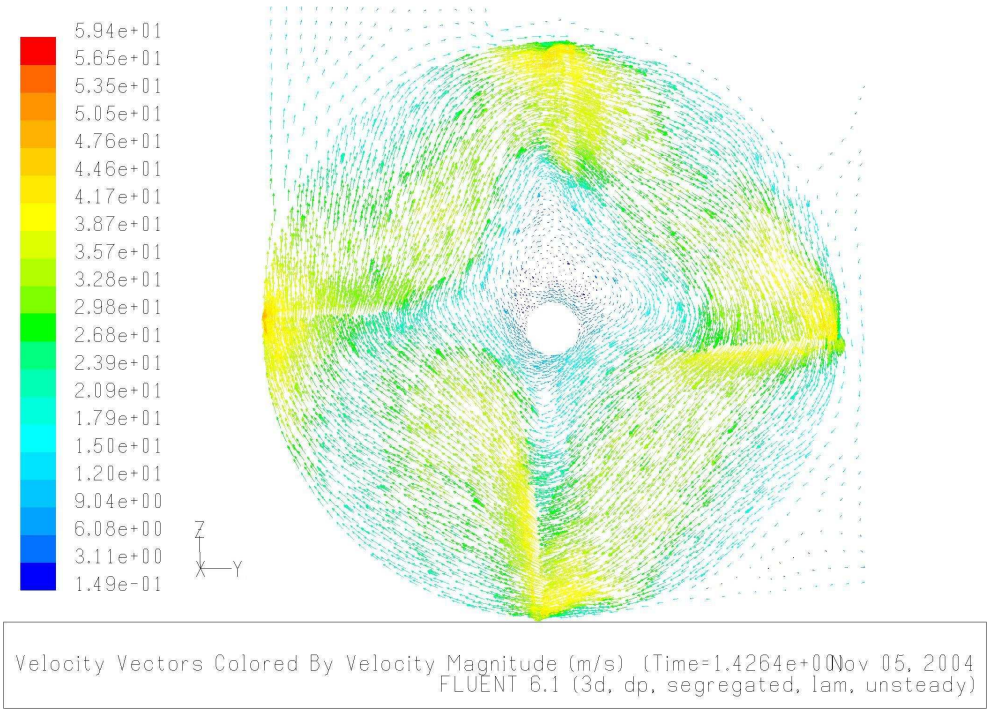

Figure 4.34 Vector plot at plane position X = -0.15 m (m/s).

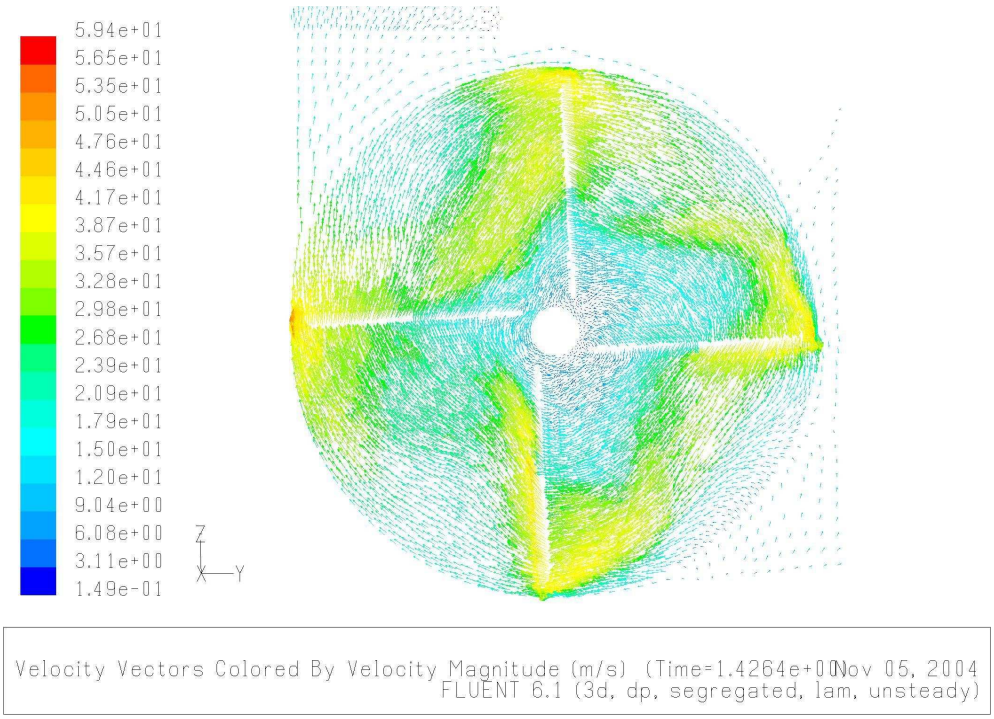

Figure 4.35 Vector plot at plane position X = -0.3 m (m/s).

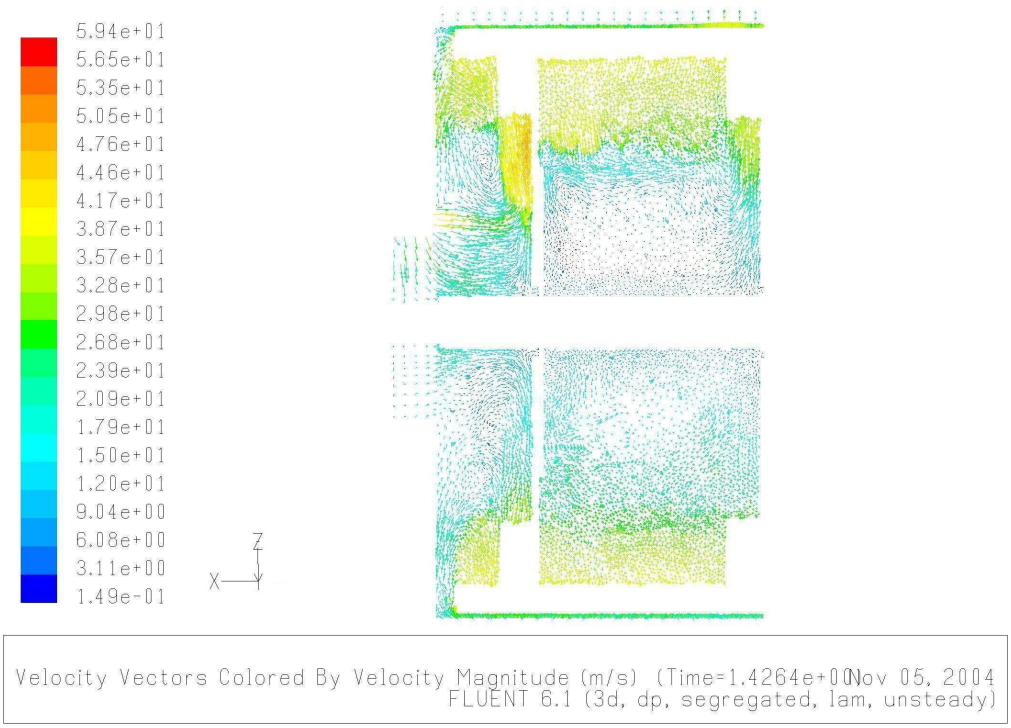

Figure 4.36 Vector plot at plane position Y = 0.0 m (m/s).

To compare the air velocities predicted by the model to the measured velocities, line surfaces were created in the model at the same position as the experimental measurement positions. Figure 4.37 shows the vertical direction velocities at the collector outlet for the measured and simulated data with 0 and 130 Pa boundary conditions. There is better agreement with the measured and simulated velocities using the 130-Pa boundary condition.

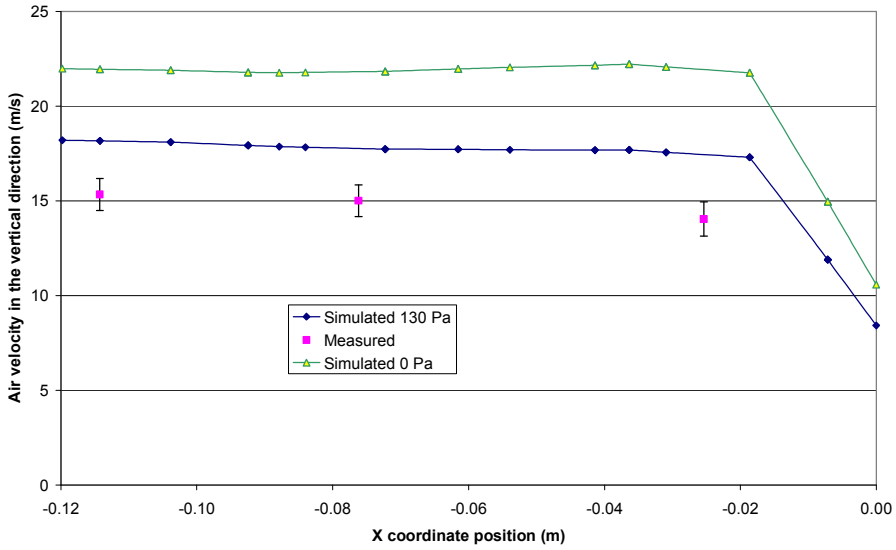

Figure 4.37 Measured and simulated vertical velocities at zone 4 using the origin given in Figure 4.28.

Figures 4.38 – 4.40 show plots of measured and simulated vertical direction velocities at each of the lettered line surfaces of zone 3 as shown in Figure 4.27. The error bars on the measured velocities are the standard deviations for each measurement. The line A plot shows a much different air flow pattern than what was measured; the simulated velocity is higher than the measured at the back of the collector and lower at the front. The line B plot shows a similar pattern as line A except slightly lower velocities and has some reverse flow as was seen in Figure 4.33. The plot of line C shows the measured and simulated velocity patterns being much closer except the measured velocities are greater with reverse flow occurring at the front of the collector again.

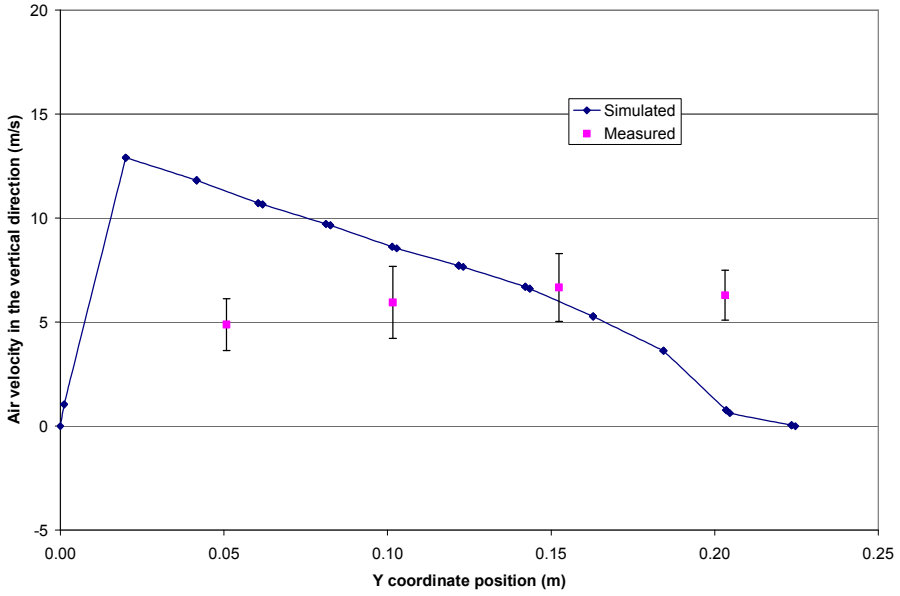

Figure 4.38 Measured and simulated vertical velocities at line A of zone 3 using the origin given in Figure 4.27.

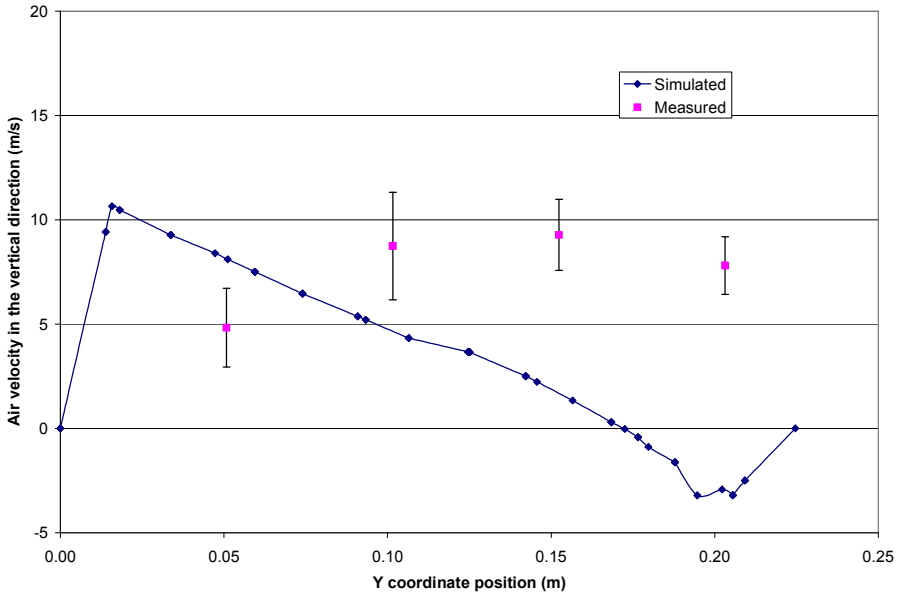

Figure 4.39 Measured and simulated vertical velocities at line B of zone 3 using the origin given in Figure 4.27.

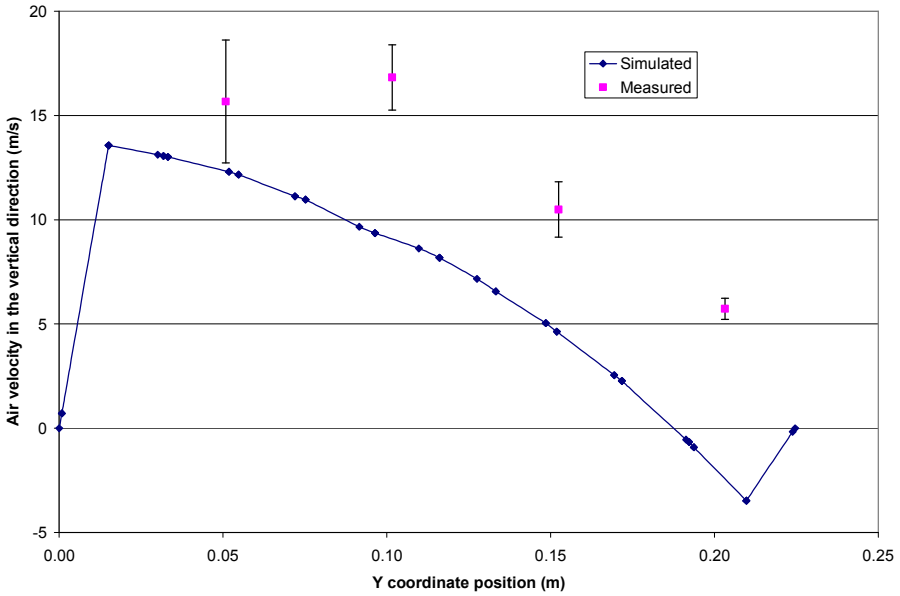

Figure 4.40 Measured and simulated vertical velocities at line C of zone 3 using the origin given in Figure 4.27.

Differences between the simulated and measured velocities could be that 1st-order discretization schemes tend to have more numerical diffusion causing the velocity to be uniform across the collector inlet instead of higher on the outside. The simulation also predicts negative velocities at the front of zone 3 which could be closer to the actual flow than what was measured because the anemometer could not differentiate between positive and negative vertical flow.

Another factor affecting the flow pattern at the collector inlet could be that only half the fan housing was modeled using a symmetry plane. This is problematic because the fan is not exactly symmetrical about the middle due to the blade support geometry. This was assumed to be negligible when designing the model but could have an effect. As well the reduced air flow on the left side caused by the fan drive pulley was not accounted for in

the model which could be a reason for the higher predicted velocities shown in Figure 4.37. A full model simulation would address these but more computing power would be needed.

4.6.2 Extension and spout

Line surfaces were also used to compare simulated and measured velocities in the extension spout model. The velocity magnitude was used because the measurement plane was not parallel to a coordinate direction. To ensure that the flow was perpendicular to the measurement plane the velocity vectors were plotted along the plane. Figures 4.41 – 4.43 show the measured velocities and the simulated velocities at the lettered line surfaces shown in Figure 4.29.

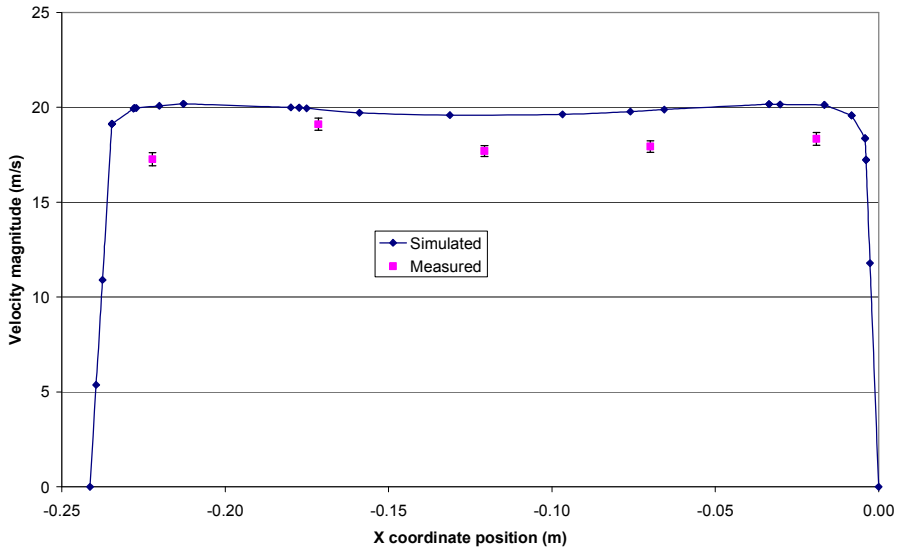

Figure 4.41 Measured and simulated velocity magnitudes at line H of zone 5 using the origin shown in Figure 4.29.

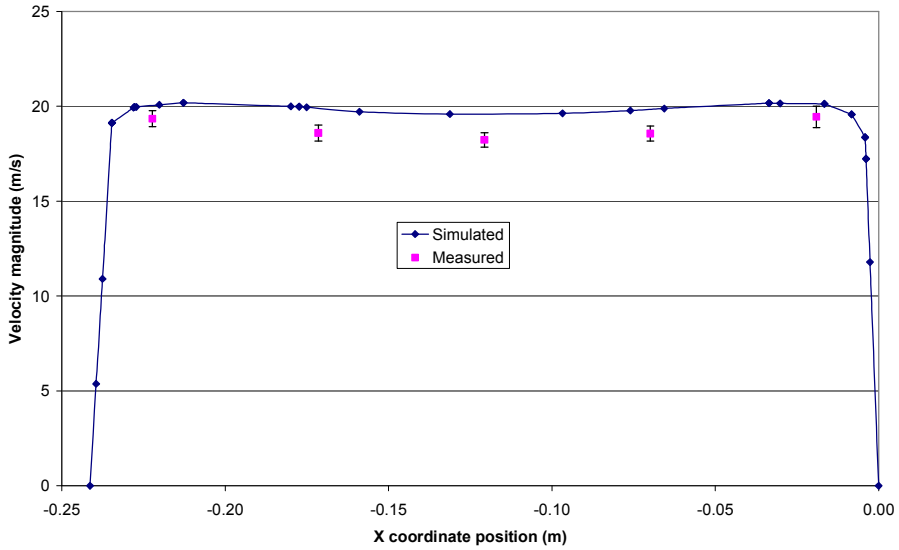

Figure 4.42 Measured and simulated velocity magnitudes at line I of zone 5 using the origin shown in Figure 4.29.

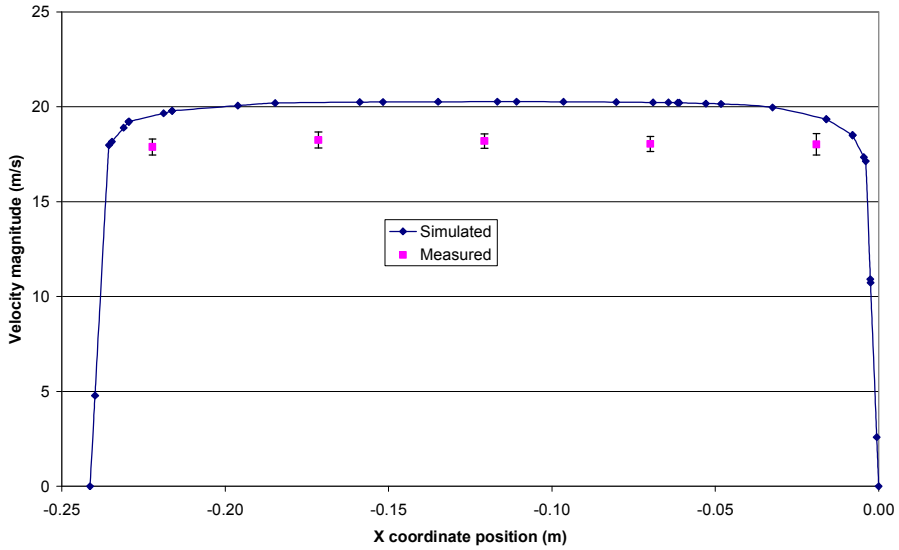

Figure 4.43 Measured and simulated velocity magnitudes at line J of zone 5 using the origin shown in Figure 4.29.

The plot of line H, I and J shows the simulated velocities being slightly greater than the measured velocities. The plots for line H and I have the general trend where the velocities are slightly less on the inside compared to the outside as seen in both the measured and simulated velocities, the exception being on the far left measured velocity of line H which is less than the other measurements. The line J plot shows the simulated velocities as slightly greater in the center of the flow while the measured velocities are approximately equal across the whole flow. The reason for the simulated velocities being greater could be due to the leakage and fasteners that were not included in the model and the fact that the walls were modeled smooth.

It was also observed that with a 15 m/s boundary condition at the extension inlet, the static pressure at that point was 130 Pa. This value was then used at the pressure outlet boundary condition on the collector outlet of the fan, housing and collector model rather than the 0 Pa used initially.

5 FORAGE FLOW MODELING

5.1 Introduction

This Chapter addresses the second and third objectives stated in Chapter 3. The development of the analytical model and prototypes will be outlined as well as the procedure for the forage velocity and throwing distance measurements. Then the model output and the experimental measurements will be compared and discussed.

5.2 Analytical Model

5.2.1 Development steps

The objective of the analytical model was to predict the distance forage would be thrown given the initial velocity of the forage as it enters the spout and the spout geometry.

The development of an analytical model of product flow within a forage harvester spout was completed in three stages. The first stage considered the energy lost as the particles impacted the curved spout at an angle. The second stage consisted of the velocity of the particles as they traveled around the curved spout. The third stage was the trajectory of the particles after they left the spout. The final velocity from each stage was passed on to the next stage and became the initial velocity for that stage. The equations from each stage were then inserted and solved in a spreadsheet.

5.2.2 Impact

An analysis was developed by Chancellor (1960) to describe the energy lost when a particle strikes a plane inclined at an angle, θ, from the initial flow direction. Assuming the impact is inelastic the particle will strike the plane as shown in Figure 5.1. The total kinetic energy lost, KE_L, is given by:

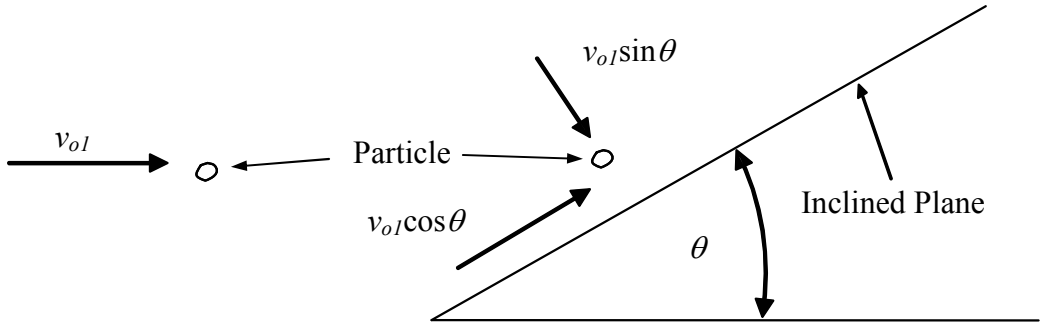

Figure 5.1 Velocity components of a particle striking an inclined plane.

$$KE_L = \tfrac{1}{2} m v_{o1}^2 \sin^2\theta + m v_{o1} \sin\theta f v_m, \tag{5.1}$$

where:
- m = mass of the particle (kg),
- v_{o1} = initial velocity of the particle (m/s),
- θ = angle of the inclined plane (radians),
- v_m = mean velocity during impact (m/s) and
- f = coefficient of friction.

The mean velocity during impact can be calculated with,

$$v_m = \frac{v_{o1}}{2}\left[-f\sin\theta + \sqrt{(f\sin\theta)^2 + 4\cos^2\theta} \right], \tag{5.2}$$

With the total kinetic energy lost known, the velocity after impact can be determined by calculating the kinetic energy of the particle before impact, subtracting the KE_L and then calculating the velocity from the final kinetic energy.

5.2.3 Velocity in the spout

The second stage of flow is described by the reduction in velocity due to friction caused by centrifugal force. Chancellor and Laduke (1960) determined that the effects of the high velocity air in an elbow could be neglected because as the flow enters the curved portion of the spout the solids are separated from the air by centrifugal action. Therefore the only forces which act on the flow of particles in the spout are the normal force, friction force between the particle and the spout and gravity. Referring to Figure 5.2 and using Newton's second law the particle motion is described by:

$$\frac{d^2 s}{dt^2} m + mg \cos\frac{s}{r} + f\left[\left(\frac{ds}{dt}\right)^2 \frac{s}{r} - mg \sin\frac{s}{r}\right] = 0\,, \tag{5.3}$$

where: s = tangential position of particle in spout measured from the horizontal (m),

g = acceleration of gravity (m/s^2),

r = radius of curvature (m) and

m = mass of particle (kg).

Equation 5.4 is the solution to Eq. 5.3 given by Chancellor and Laduke (1960),

$$v^2 = \frac{2gr\left[\left(\sin\frac{s}{r}\right)\left(2f^2-1\right)-\left(3f\cos\frac{s}{r}\right)\right]}{4f^2+1} + C\exp\left[-\frac{2fs}{r}\right] \text{ and} \tag{5.4}$$

$$C = \frac{v_{02}^2 - \dfrac{2gr\left[\left(\sin\frac{s_0}{r}\right)\left(2f^2-1\right)-\left(3f\cos\frac{s_0}{r}\right)\right]}{4f^2+1}}{\exp\left[-\dfrac{2fs_0}{r}\right]} \tag{5.5}$$

where: v_{o2} = initial tangential velocity of the particle (m/s) and

s_o = initial tangential position of particle in spout measured from the horizontal (m).

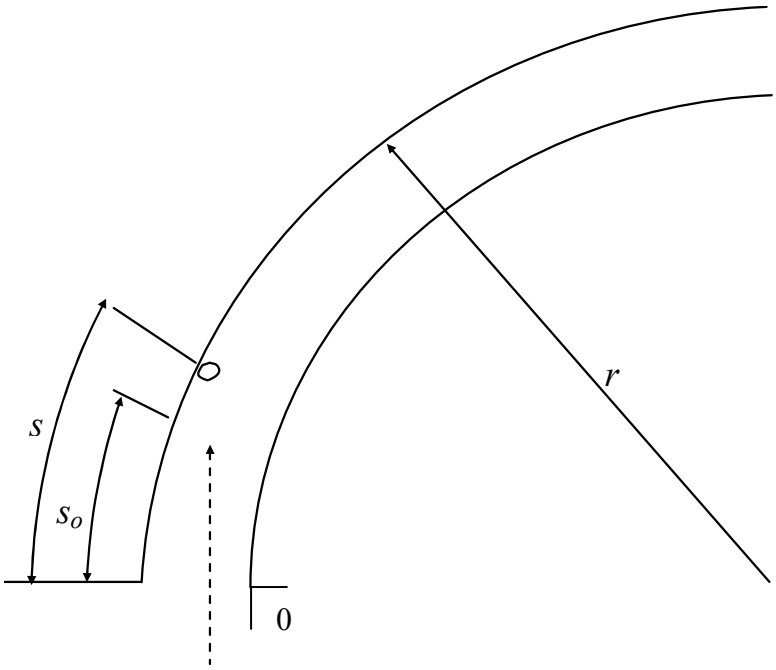

Figure 5.2 Variables used to describe particle movement in the spout.

5.2.4 Particles leaving the spout

To determine the path (*x,y*) of the particles after they leave the spout, the laws of inclined throw are utilized with allowance for aerodynamic resistance. The following is a summary of the method given in Sitkei (1986).

The particles leave the spout at an initial velocity, v_{o3} (m/s), and at some angle, α_{throw} (radians), as measured from the horizontal (Figure. 5.3).

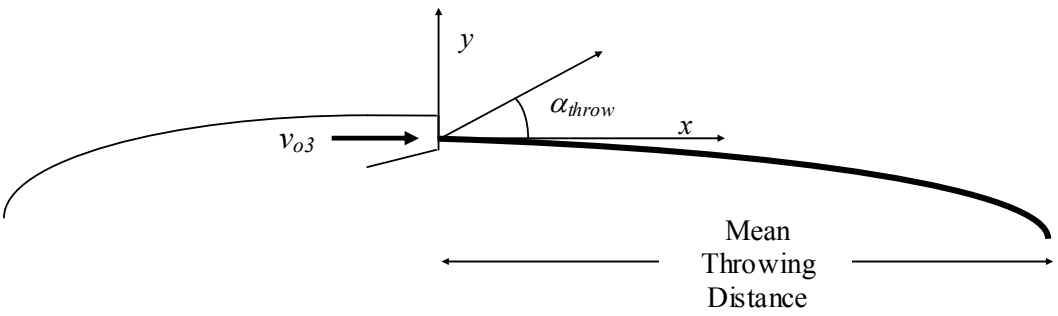

Figure 5.3 Variables used to describe the particles leaving the spout.

This velocity can then be decomposed into horizontal and vertical components,

$$v_{03} = \sqrt{\dot{x}^2 + \dot{y}^2} = \sqrt{\left(\frac{dx}{dt}\right)^2 + \left(\frac{dy}{dt}\right)^2}, \tag{5.6}$$

where: x = horizontal position (m) and

y = vertical position (m).

A particle placed into a flowing medium is subject to a force due to the asymmetrical pressure distribution, termed the aerodynamic or drag force. The drag force, W_{df} (N), or aerodynamic resistance from the blower on a given body may be calculated from Eq. 5.7,

$$\vec{W}_{df} = c_w A_p \left(\frac{\rho_A}{2g}\right) v_{03}^2, \tag{5.7}$$

where c_w = drag coefficient,

A_p = cross sectional area of the body normal to the flow (m^2) and

ρ_A = air density (kg/m^3).

Decomposition of the drag force into horizontal and vertical components gives,

$$W_x = W_{df} \cos\alpha_{throw} \text{ and} \tag{5.8}$$

$$W_y = W_{df} \sin\alpha_{throw}, \tag{5.9}$$

where: W_x = horizontal component of drag force (N) and

W_y = vertical component of drag force (N),

both of which would be negative with respect to the coordinate system in Figure 5.3.

The horizontal and vertical components of v_{03} can be rearranged to form:

$$\cos\alpha_{throw} = \frac{\frac{dx}{dt}}{v_{03}} \text{ and} \tag{5.10}$$

$$\sin\alpha_{throw} = \frac{\frac{dy}{dt}}{v_{03}}. \tag{5.11}$$

The only force acting on the particle in the x direction is the horizontal component of the drag force, so applying Newton's second law gives:

$$m\frac{d^2x}{dt^2} = -W_x. \tag{5.12}$$

Combining Eqs. 5.7, 5.8 and 5.10 gives:

$$m\frac{d^2x}{dt^2} = -c_w A_p\left(\frac{\rho_A}{2g}\right)v_{03}^2\left(\frac{\frac{dx}{dt}}{v_{03}}\right). \tag{5.13}$$

Simplifying and substituting in Eq. 5.6 gives:

$$m\frac{d^2x}{dt^2} = -K_1\frac{dx}{dt}\sqrt{\left(\frac{dx}{dt}\right)^2 + \left(\frac{dy}{dt}\right)^2}, \tag{5.14}$$

where: $$K_1 = c_w A_p\left(\rho_A \big/ 2g\right).$$

Following the same procedure in the y direction as in the x direction and taking gravity into account gives:

$$m\frac{d^2y}{dt^2} = -K_1\frac{dy}{dt}\sqrt{\left(\frac{dx}{dt}\right)^2 + \left(\frac{dy}{dt}\right)^2} - mg. \tag{5.15}$$

A large proportion of agricultural products are irregular bodies (like silage); in this case the drag coefficient depends also on the shape and instantaneous position (orientation). Generally, an equivalent diameter of a sphere is used to calculate the projected cross-sectional area.

In the case of spherical particles the cross-sectional area, A_p, and mass, m, may be expressed in terms of the diameter, giving the differential equations:

$$\ddot{x} = -K\ \dot{x}\sqrt{\dot{x}^2 + \dot{y}^2} \quad \text{and} \tag{5.16}$$

$$\ddot{y} = -g - K\dot{y}\sqrt{\dot{x}^2 + \dot{y}^2}\ , \tag{5.17}$$

where:

$$K = \frac{3\rho_A c_w}{4\nu_{dens} d_A} = \text{aerodynamic coefficient (m}^{-1}\text{)},$$

ν_{dens} = density of particles (kg/m^3) and

d_A = mean equivalent diameter of particle (m).

The solution of Eqs. 5.16 and 5.17 for the position *(x,y)* at the center of the flow of the silage particles is given by:

$$x = \frac{m}{K} v_{03} \left(1 - e^{\frac{-K}{m}t}\right) \cos\alpha_{throw} \quad \text{and} \tag{5.18}$$

$$y = \frac{m}{K}\left(\frac{m}{K} g + v_{03} \sin\alpha_{throw}\right)\left(1 - e^{\frac{-K}{m}t}\right) - \frac{m}{K} gt\ . \tag{5.19}$$

5.2.5 Spreadsheet model

The equations described above were solved in a spreadsheet. Each stage was completed separately having an initial velocity entering and a final velocity. The first impact stage required the input of the initial velocity of the forage as it enters the spout and the friction

coefficient. The geometry of the spout determines the angle of impact. From these the velocity of forage after the impact is known and used as the initial velocity for the second stage.

For the velocity in the spout, the geometry determines the initial position, radius of curvature and final position. From these and the friction coefficient the equations give the velocity at the end of the curvature. This is passed on as the initial velocity for the second radius and the same procedure gives the velocity of the forage as it enters the second impact.

The second impact is solved with the same method as the first giving the initial velocity for the throwing distance equations. An aerodynamic coefficient of 6 m^{-1} was used along with a mass value of 5 kg. These values were estimated and may not reflect actual values and did not affect the prototype development because the prototypes were designed to maximize the exit velocities at the end of the spout. Using these values the vertical and horizontal positions of the forage stream was calculated at a time increment of 0.0075 s. When the magnitude of the vertical position of the forage stream was equal to the distance between the end of the spout and the ground, the horizontal position was then the predicted throwing distance.

5.3 Prototype Development

The two prototype spout designs were developed using the analytical model. The equations were solved in a spreadsheet so different spout dimensions could be compared. Most of the dimensions for the prototype spouts were determined by trial and error. The

vertical height of the curvature of the spout was kept at 1.17 m (46 in), the same as the current design. The exit angle for the prototypes was set at 15° at the request of the manufacturer. Other dimensions such as angle of attack, radii of curvatures and lengths of curvatures were adjusted to achieve the maximum throwing distance.

Figure 5.4 shows the dimensions of the current spout and the positions of the attack, impact and exit angles and the separation distance. The impact angle was the measurement between the tangent of the curve and the vertical direction directly above the center of the cylindrical spout extension. The attack angle was the measurement between the tangent of the beginning of the spout curvature and the vertical direction. The exit angle was measured between the tangent of the end of the spout curvature and the horizontal direction. The separation distance was the vertical distance between the beginning of the spout curvature and the forage impact position.

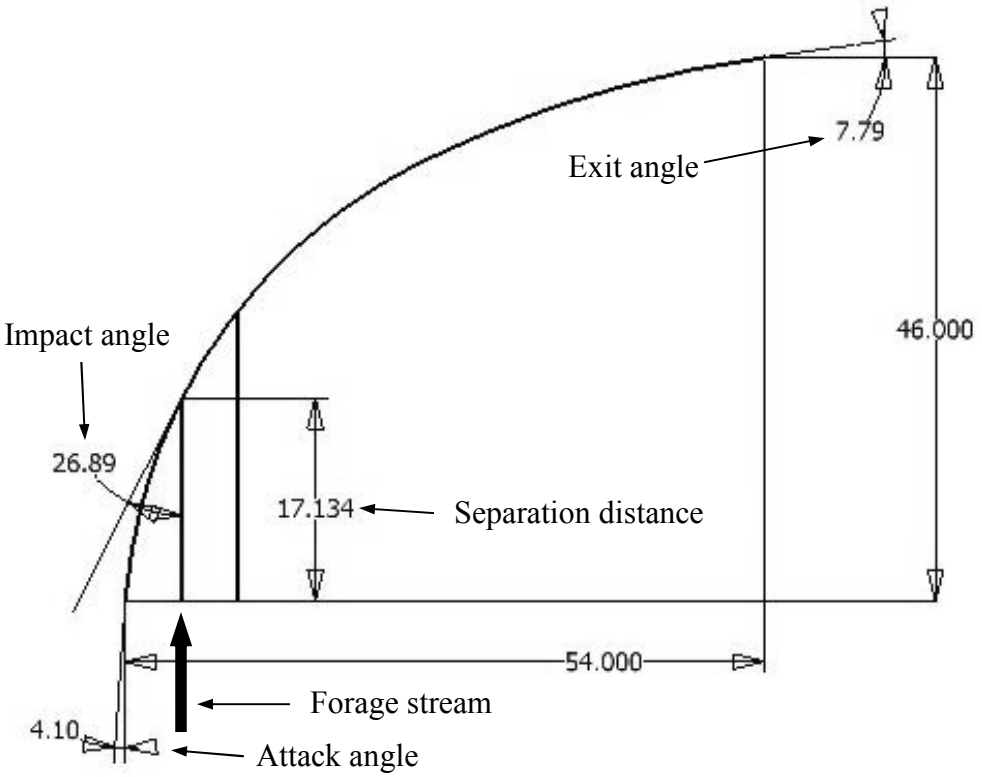

Figure 5.4 Current spout's dimensions values and locations (in).

To increase the throwing distance the initial angle of impact was reduced to lower the energy lost during impact as suggested by Chancellor (1960), but after consultation with the manufacturer, it was decided that increasing the angle of attack to make the forage separate from the air stream sooner was more important because this was the method used by industry in the past. Sooner separation of the forage from the air stream should reduce the drag due to the velocity of the air being less than the forage. Therefore the prototypes were designed to have earlier separation while maintaining as small an impact angle as possible. Table 5.1 shows the major dimensions of the current and prototype spouts named P1 and D1.

Table 5.1: Comparison of the major spout dimensions of the current, P1 and D1 spouts.

Spout	Attack Angle (°)	Impact Angle (°)	Exit Angle (°)	Separation Distance (in)	Arc Length (in)
Current	4.1	26.9	7.8	17.13	59.42
P1	10.0	27.2	15.0	14.10	62.24
D1	18.0	28.0	15.0	11.21	57.46

5.4 Forage Velocity Measurement

To obtain initial conditions and attempt to validate the analytical model, a method of measuring the velocity of the forage in the spout was needed.

5.4.1 Materials and methods

The method of measuring the forage velocity involved the use of a high speed camera to film the flow of forage in the spout. Filming required the removal of portions of the spout and collector and replacing it with clear plastic windows.

The forage harvester was powered by an 8670 New Holland tractor rated at 108 pto kW (145 pto hp). Tests needed to be conducted with the forage harvester stationary so that forage could be filmed. Therefore a conveyor powered by the tractor hydraulics was used to feed whole corn stalks into the harvester.

With viewing windows in place, the flow of forage was filmed in three different positions; the side of the collector, the back of the collector and the beginning of the spout. A high-speed camera (MotionMeter, Redlake, San Diego, CA) was used to record the video at a frame rate of 500 frames per second (fps). The camera was mounted on a forklift (Figure 5.5) to hold the camera still and to allow easier positioning when filming

the spout due to the spout's height. The camera stored images in internal memory that were then played back at 30 fps and recorded to the hard drive of a computer at the same frame rate. A software program was then used to extract individual frames allowing particle velocities to be calculated.

Figure 5.5 High-speed camera mounted on forklift.

The velocity of the forage was calculated by measuring the distance that the forage traveled between consecutive frames, then dividing that distance by the time between each frame as determined by the frame rate. In the experiments conducted for this project a frame rate of 500 fps was used, making the time between consecutive frames 0.002 s. AutoCAD 2002 was used to measure the distance the forage traveled. The individual frames were imported into the program and then scaled to actual size. Measurements were then made to a common base point to get the distance traveled between consecutive frames.

5.4.2 Results

The video obtained during experiments was not as useful as expected. It was found that it was very hard to distinguish forage particles between consecutive frames. Therefore groups or clumps of particles had to be followed. The most successful videos were those taken at the back of the collector. Here, the forage particles were still tightly packed together after leaving the fan blade and could be easily followed in consecutive frames as shown in Figure 5.6.

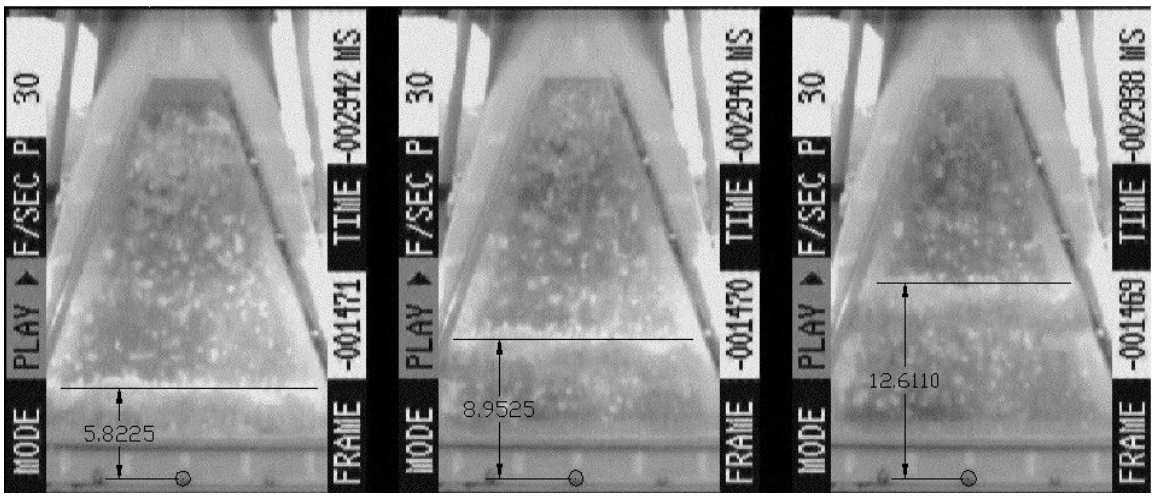

Figure 5.6 Forage velocity measurement at the back of collector using high-speed camera.

The video taken at the beginning of the spout was more difficult to use for velocity calculations. The collector converged to a narrow opening at the top and the tightly packed particles leaving the fan blade tended to become a steady stream, therefore velocity measurements were limited to frames that had a large clump traveling upwards in the spout as shown in Figure 5.7.

Figure 5.7 Forage velocity measurement at the beginning of the spout using high-speed camera.

When a series of frames could be measured, it was found that three images could be recorded before the forage impacted the spout. This then gave two distance differences and therefore two velocity measurements that were then averaged together. This was completed for three sets of frames to calculate an average speed of 45 m/s.

It was found that measurement of forage velocities after their impact on the spout was impossible using high-speed photography. This was due to the fact that the plexiglas on the sides of the spout did not extend all the way to the outer edge of the spout, leaving approximately 2 cm of steel that obstructed the view of the forage flow.

5.5 Throwing Distance Measurement

To validate the analytical model, a method of measuring the distance that forage was thrown from the end of the spout was needed.

5.5.1 Materials and methods

The mean throwing distance after the forage leaves the spout can be measured using the same technique that was used by Shinners et al. (1994). They compared the throwing distance of two forage harvesters. The forage harvesters remained stationary and crop

was fed into the machine using a conveyor. A 16.5-m long plastic strip was placed on the ground behind each machine. The start of the strip was placed directly under the end of the spout and the rest of the strip was divided into eleven 1.5-m sections. After each test, the mass of material in each of the 11 sections was determined. Then, calculating the percentage of total mass in each section produced a material distribution curve. From this curve a mean and standard deviation of throwing distance were calculated.

Roberge et al. (1997) used a similar method for throwing distance measurements, the difference here being that the tests performed were not stationary but done in the field. To accommodate this, a forage wagon towed behind the harvester was divided into separate sections that allowed the calculation of the throwing distance as described above but the section walls interfered with the crop trajectory and underestimated the results.

It should be noted that the mean throwing distance of the forage harvester is dependent on the height of the horizontal plane on which it is measured. Therefore the mean throwing distance as measured at ground level would be greater than if it was measured at the floor level of a forage wagon. For this project the mean throwing distance was used to compare different spout geometries and does not predict how far each spout would throw into a wagon or truck.

Throwing distance tests for this project were completed in Québec where a conveyor was not available to feed crop into the harvester for stationary tests. Therefore tests had to be completed in the field. The same concept as above was used except a tarp was pulled

behind the forage harvester to collect the forage in the marked off sections as shown in Figure 5.8, which eliminated the wall interference found when using a forage wagon.

Wind speed and direction can have an effect on the measured throwing distance during testing. Ideally testing should be completed under zero wind conditions. However due to time and crop maturity the tests had to be completed with wind present. The day the testing was completed the wind speed ranged from 13 to 26 km/h as measured at the Quebec City Jean Lesage International Airport, which was approximately 10 km from the test site. The wind direction ranged from 220° to 270°, as measured from due north in a clockwise direction, with the windrow direction being approximately 220°.

Figure 5.8 Throwing distance test configuration.

The throwing distance of three spout designs was measured; the current production model and two prototype designs were developed using the analytical model described in Section 5.2. The forage harvester was a Dion model 1224 with an 800-rpm gear box and

was powered by a Fendt 924 tractor rated at 179 pto kW (240 pto hp). The crop was a mixture of timothy and other grasses and was cut the morning of the tests. Tests were completed in the afternoon by harvesting a measured 12.2 m (40 ft) section of a windrow at a constant speed of 6.4 km/h (4 mph). The weight of the forage in each 1-m section, as marked on the tarp, was recorded. After each spout test, a sample of the chopped forage was collected for moisture measurement.

The geometric mean throwing distance and standard deviation could then be calculated using the following equations:

$$x_{gm} = \log^{-1}\left[\frac{\sum\left(M_i \log x_{ai}\right)}{\sum M_i}\right] \text{ and} \tag{5.20}$$

$$S_{gm} = \log^{-1}\left[\frac{\sum_{i=1}^{n}\left[M_i\left(\log x_{ai} - \log x_{gm}\right)^2\right]}{\sum M_i}\right]^{-1/2} \tag{5.21}$$

where: x_{gm} = geometric mean throwing distance (m),

s_{gm} = geometric standard deviation (m),

M_i = mass in each section (percent of total) (kg) and

x_{ai} = midpoint throwing distance of each section (m).

5.5.2 Results and discussion

Table 5.2 shows the results of the throwing distance experiments. The results show that there was not a statistically significant difference between the throwing distances of the three spout designs.

Table 5.2: Results of throwing distance tests for current, P1 and D1 spouts.

Spout	Geometric mean throwing distance (m)	Throwing distance geometric standard deviation	Replicates
Current	9.25_a	1.20_a	3
P1	8.03_a	1.21_a	4
D1	8.89_a	1.19_a	3

Averages with the same subscript are not significantly different

The likely reason the prototype designs did not throw further than the current design was due to the positioning of the deflector at the end of the spout. For all tests the deflector was positioned so it was horizontal with the frame of the forage harvester. This position caused the forage to have a larger impact with the deflector for the prototype designs compared to the current design. The angle with respect to the horizontal at the end of the spout for both the prototypes was 15° while the current design was 8°.

5.6 Validation

To account for the impact at the end of the spout due to the deflector, a second impact calculation was added to the analytical model. This allowed the predicted mean throwing distances to be compared to the measured mean throwing distances. This was completed by adjusting the aerodynamic coefficient so the predicted and measured throwing

distances were equal for the current spout. Table 5.3 shows the comparison of the theoretical and measured throwing distances.

Table 5.3: Theoretical and experimental throwing distance comparison.

	Mean Throwing Distance (m)		
	Current	D-1	P-1
Theoretical	9.25	8.68	8.97
Experimental	9.25	8.89	8.03

The analytical model under-predicted with respect to the D-1 prototype by 2% and over-predicted the P-1 prototype by 12 %. To understand why this occurs would require further testing with a method of measuring the velocity of forage as it leaves the spout such as Doppler radar. This would allow the model to be split into two parts; then it could be determined which part is accurate.

6 CONCLUSIONS

With the overall objective of increasing the throwing distance of a pull-type forage harvester, two models were developed: a numerical model which utilized FLUENT (CFD software) to predict air velocities in the blower and spout and an analytical model to predict the mean throwing distance of the forage harvester.

- Both the numerical and analytical models were successfully developed.
- Comparison of the numerical model results to experimental air velocity measurements showed that the fan portion of the model was on the same order of magnitude but flow patterns differed. The spout portion of the model was able to accurately simulate the actual air velocities.
- From the analytical model two prototype spouts were developed and tested. The results found that there was not a statistically significant difference between the throwing distances of the three spouts.

7 REFERENCES

Aarseth, K.A. 2004. Attrition of feed pellets during pneumatic conveying: the influence of velocity and bend radius. *Biosytems Engineering*. 89(2):197-213.

Baker, J.D. and G.E. Klinzing. 1999. Optimal performance of pneumatic transport systems. *Powder Technology*. 104:240-247.

Chancellor, W.J. 1960. Influence of particle movement on energy losses in an impeller blower. *Agricultural Engineering*. 41(2):92-94.

Chancellor, W.J. and G.E. Laduke. 1960. Analysis of forage flow in a deflector elbow. *Agricultural Engineering*. 41(4):234-236, 240.

FLUENT. 2003. *FLUENT 6.1 User's Guide*. Lebanon, NH.

FLUENT. 2005. *Overview of turbulence modeling*. From http://www.learningcfd.com/login/fluent/advanced/lectures/turbulence/adv-turb-v62_01_overview.pdf.

Kepner, R.A., R. Bainer and E.L. Barger. 1978. *Principles of farm machinery*, 3rd edition. Westport, CT: AVI Publishing Company Inc.

Lee, L.Y., T.Y. Quek, R. Deng, M.B. Ray and C. Wang. 2004. Pneumatic transport of granular materials through a 90° bend. *Chemical Engineering Science*. 59:4637-4651.

Levy, A. and D.J. Mason. 1998. The effect of a bend on the particle cross-section concentration and segregation in pneumatic conveying systems. *Powder Technology*. 98:95-103.

Mason, D.J., P. Marjanovic and A. Levy. A simulation system for pneumatic conveying systems. *Powder Technology*. 95:7-14.

Nieuwenhof, P. 2003. Modeling of the energy requirements of a non-row sensitive corn header for a pull-type forage harvester. Unpublished M.Sc. Thesis. University of Saskatchewan.

Reznik, N.E. 1966. Forage harvester design (translation). *Traktory I selkhozmashiny*. 2:28-32.

Roberge, M., P. Savoie and E. Norris. 1997. Throwing capacity of a pull-type forage harvester using a crop processor. Proceedings of the Canadian Society of Agricultural Engineering Annual Conference, May 28-30, Sherbrooke, Vol. A 405-414, Saskatoon, SK, CSAE.

Shinners, K.J., R.G. Koegel and P.J. Pritzl. 1991a. An upward cutting cut-and-throw forage harvester to reduce machine energy requirements. *Transactions of the ASAE*. 34(6):2287-2290.

Shinners, K.J., R.G. Koegel, P.J. Pritzl and L.L. Lehman. 1991b. Band lubrication to reduce friction loss in forage blowers. *Transactions of the ASAE*. 34(5):1962-1966.

Shinners, K.J., M. Stelzle and R.G. Koegel. 1994. Improving the throwing effectiveness of an upward-cutting forage harvester. *Transactions of the ASAE*. 37(4):1059-1067.

Sitkei, G. 1986. *Mechanics of agricultural materials*. Elsevier, New York, NY.

Stoess, H.A. 1983. *Pneumatic conveying*, 2nd edition. New York, NY: John Wiley & Sons Inc.

Totten, D.S. and W.F. Millier. 1966. Energy and particle path analysis: forage blowers and vertical pipe. *Transactions of the ASAE*. 9(5):629-636, 640.

Tremblay, D., P. Savoie and Q. Le Phat. 1991. Reducing forage harvester peak power with a flywheel. *Applied Engineering in Agriculture*. 7(1):41–45.

8 APPENDIX A

Appendix A: Air velocity measurement data

Table A-1: Average air velocities from zone 1 measured from the origin in Figure 4.25 (m/s).

		Width (m)			
		-0.05	-0.10	-0.15	-0.20
Height (m)	0.36	12.43	16.61	21.14	21.49
	0.29	7.21	11.04	8.95	8.60
	0.21	8.95	14.18	13.83	13.13
	0.14	8.26	15.22	13.83	14.18
	0.06	6.86	6.52	5.82	6.52

Table A-2: Standard deviation of air velocities from zone 1 measured from the origin in Figure 4.25 (m/s)

		Width (m)			
		-0.05	-0.10	-0.15	-0.20
Height (m)	0.36	2.63	2.63	1.60	1.04
	0.29	1.60	1.04	1.04	0.60
	0.21	1.04	1.04	1.60	1.04
	0.14	0.60	1.04	1.60	1.04
	0.06	1.04	0.60	1.04	0.60

Table A-3: Average air velocities from zone 2 (m/s)

	Average
Top	9.83

		Average
Side Top to Bottom (m)	0.03	6.68
	0.10	7.91
	0.16	7.64

Table A-4: Standard deviation of air velocities from zone 2 (m/s)

	STDEV
Top	6.66

		STDEV
Side Top to Bottom (m)	0.03	0.85
	0.10	0.24
	0.16	0.24

Table A-5: Average air velocities from zone 3 measured from the origin in Figure 4.27 (m/s)

		Width (m)				
		-0.02	-0.17	-0.31	-0.46	-0.60
Depth-Back to Front (m)	0.05	15.674	4.826	4.881	4.248	12.08
	0.10	16.826	8.740	5.951	5.731	13.79
	0.15	10.492	9.270	6.664	6.503	8.652
	0.20	5.7295	7.803	6.291	6.618	4.767

Table A-6: Standard deviation of air velocities from zone 3 from the origin in Figure 4.27 (m/s)

		Width (m)				
		-0.02	-0.17	-0.31	-0.46	-0.60
Depth-Back to Front (cm)	0.05	2.953	1.885	1.253	0.853	2.258
	0.10	1.565	2.584	1.727	1.254	1.593
	0.15	1.329	1.705	1.631	1.179	0.972
	0.20	0.505	1.376	1.200	0.73	0.414

Table A-7: Average air velocities from zone 4 measured from the origin in Figure 4.28 (m/s)

Width (m)				
-0.03	-0.08	-0.11	-0.15	-0.20
14.037	15.005	15.336	16.026	13.693

Table A-8: Standard deviation of air velocities from zone 4 measured from the origin in Figure 4.28 (m/s)

Width (m)				
-0.03	-0.08	-0.11	-0.15	-0.20
0.909	0.832	0.846	0.841	0.984

Table A-9: Average air velocities from zone 5 measured from the origin in Figure 4.29 (m/s)

		Width (m)				
		-0.02	-0.07	-0.12	-0.17	-0.22
Depth - Outside to Inside (m)	0.03	18.340	17.940	17.703	19.105	17.268
	0.08	19.440	18.560	18.232	18.590	19.339
	0.13	18.030	18.050	18.200	18.249	17.885

Table A-10: Standard deviation of air velocities from zone 5 measured from the origin in Figure 4.29 (m/s)

		Width (m)				
		-0.02	-0.07	-0.12	-0.17	-0.22
Depth - Outside to Inside (m)	0.03	0.328	0.301	0.290	0.319	0.348
	0.08	0.566	0.396	0.377	0.418	0.424
	0.13	0.392	0.411	0.509	0.636	0.350